Experimental observations on the creep behaviour of frozen soil

Katarzyna Staszewska*, Andrzej Niemunis**, Marcin Cudny
Faculty of Civil and Environmental Engineering, Gdańsk University of Technology, Poland

Abstract

Constitutive models in the literature for creep of frozen soil are based on the direct use of time counted from the onset of creep. An explicit time dependence in a constitutive equation violates the principles of rational mechanics. No change in stress or temperature is allowed for during creep, using the time-based formulations. Moreover, the existing descriptions need much verification and improvement on the experimental side as well.

Creep behaviour of artificially frozen sand was evaluated experimentally. Novel testing methods were used and new insights into the creep behaviour of frozen soil were gained.

Creep rate under uniaxial compression was examined with different kinds of interruptions, like unloadings or overloadings. Experimental creep curves were presented as functions of creep strain. They were brought to a dimensionless form which describes the creep universally, despite changes in stress or temperature. Possible anisotropy of frozen soil was revealed in the creep tests on cubic samples with changes of the loading direction. Using the particle image velocimetry (PIV) technique, information on the lateral deformation and the uniformity of creep were obtained. Volumetric creep of unsaturated frozen soil under isotropic compression was demonstrated to be due to the presence of air bubbles only.

Keywords: creep, rate dependence, artificially frozen sand, uniaxial compression, anisotropy, PIV, dilatancy, isotropic compression

*Corresponding author
**Institute of Soil Mechanics and Rock Mechanics, Karlsruhe Institute of Technology, Germany
Email addresses: katstasz@pg.edu.pl (Katarzyna Staszewska), andrzej.niemunis@kit.edu (Andrzej Niemunis), mcud@pg.edu.pl (Marcin Cudny)

1. Introduction

Artificial ground freezing is a technique used as a temporary soil stabilisation and insulation method, e.g., during tunnel constructions in urban areas. It often turns out to be the most efficient and environmental friendly solution to provide a temporary earth support [18]. In most cases, the creep of frozen soil, rather than its short-term strength, is of the primary importance. Present evaluation of the creep deformation of frozen soil is oversimplified. High safety factors or basing on the engineering experience are commonly applied. This can result in expensive design or in geotechnical failures. A recent example of such failure is the collapse of a tunnel in Rastatt, Germany [8]. It indicates that the mechanical behaviour of frozen soil is not well understood as yet.

The most popular currently used mathematical description of creep in frozen soil [2, 3, 17] is non-autonomous as it is explicitly dependent on the time elapsed from the onset of creep. The efficiency and safety of the ground freezing technology could be increased by incorporation of a sound theoretical model. A new state variable that dictates the rate of creep and ensures the autonomy of constitutive description should be developed. Novel aspects, like the volumetric creep and anisotropy of frozen soil, should be experimentally investigated and included into such model.

In geomechanics, there is no generally accepted set of state variables that governs the rate of creep in frozen soil except for the stress, $\boldsymbol{\sigma}$, the temperature, Θ, and the void ratio, e. In clayey soil at positive temperatures, such variable is the overconsolidation ratio, OCR. It is not easy, however, to adopt the creep rate $\dot{\boldsymbol{\varepsilon}}^{\mathrm{vp}}(\mathrm{OCR})$ known from [24] for frozen soil because the concept of the effective stress in frozen soil has not been established as yet. Besides, the OCR-based models are not capable to describe the tertiary creep.

To develop a novel constitutive framework, the creep of frozen sand was inspected in the frost laboratory at the Institute of Soil Mechanics and Rock Mechanics (IBF) at the Karlsruhe Institute of Technology (KIT). Based on the new experimental observations, the shortcoming of direct time dependence is evident. Simulation of creep with interruptions, like unloadings or overloadings, using an explicit time function is impossible.

Present state of the art on the creep behaviour of frozen soil is given as first. Novel experiments required for the formulation of an improved creep description are then described and their results are reported. Finally, the essential lab observations are summarised.

Notation

Bold-face letters, like $\boldsymbol{\sigma}$, are second rank tensors. The geotechnical sign convention with compression positive is applied to stress $\boldsymbol{\sigma}$ and strain $\boldsymbol{\varepsilon}$. The elastic part of strain is denoted as $\boldsymbol{\varepsilon}^{\mathrm{el}}$ and the visco-plastic one as $\boldsymbol{\varepsilon}^{\mathrm{vp}}$. Uniaxial stress is understood as diagonal form $\boldsymbol{\sigma} = \mathrm{diag}(\sigma, 0, 0)$. The basic variables are given below.

e	void ratio
E, K	elastic constants
p	isotropic pressure
S	degree of saturation
t	time
t_m	standing time
$\mathbf{u}(\mathbf{X}, t)$	displacement field in material description
V	volume
$\mathbf{X}$	reference location
$\boldsymbol{\varepsilon}$	strain tensor (compression positive)
$\boldsymbol{\varepsilon}(\mathbf{X}, t)$	deformation field in material description
$\varepsilon^{\mathrm{vp}}$	visco-plastic strain measured in creep tests under uniaxial stress
ε_m	creep strain at $\dot{\varepsilon}_m$
$\dot{\varepsilon}_m$	minimum creep rate
$\varepsilon_{\mathrm{vol}}$	volumetric strain $\varepsilon_{\mathrm{vol}} = \mathrm{tr}\,\boldsymbol{\varepsilon}$
$\varepsilon_{\mathrm{vol\,max}}$	maximum volumetric creep strain
$\mu^{\sqcup}$	volumetric content of $\sqcup$, $\mu^{\sqcup} = V^{\sqcup}/V$
$\boldsymbol{\sigma}$	total stress tensor (compression positive)
σ	component of uniaxial stress $\boldsymbol{\sigma} = \mathrm{diag}(\sigma, 0, 0)$
$\boldsymbol{\sigma}^{\mathrm{eff}}$	effective stress in soil skeleton
Θ	temperature [°C]

$\dot{\sqcup}$	material rate of $\sqcup$, $\dot{\sqcup} = \partial \sqcup / \partial t = \sqcup_{,t}$
$\sqcup_{\text{hor}}, \sqcup_{\text{vert}}$	horizontal and vertical component
$\operatorname{tr} \sqcup$	trace of $\sqcup$, e.g., $\operatorname{tr} \boldsymbol{\sigma} = \sigma_{ii}$

The essential abbreviations are listed below.

A	cubic (suited for testing of anisotropy) frozen sample tested without the PIV
AF	cubic (suited for testing of anisotropy) frozen sample tested with the PIV (i.e., ger *fotografiert*)
C	standard (uninterrupted) creep test
CurC	creep test with an unloading-reloading cycle followed by creep
CoC	creep test with an overloading followed by creep
CoCrC	creep test with an overloading followed by creep, reloading and creep
CA	creep test with a change of the loading direction (for examination of anisotropy)
CI	creep test under isotropic compression
CSR	constant strain rate
KFS	Karlsruhe Fine Sand
KS	cylindrical sample in a creep test (ger *Kriechtest*) on frozen sand
PIV	particle image velocimetry

2. Creep of frozen soil

Three stages of creep are defined for frozen soil, Fig. 1a, judging by the deformation rate as a function of time:

- *primary* (decreasing)
- *secondary* (constant)
- *tertiary* (increasing),

see Fig. 1b. One interpretes the secondary stage as an inflection point of the $\varepsilon^{\text{vp}} - t$ plot (with the corresponding minimum of the $\dot{\varepsilon}^{\text{vp}} - t$ plot) [17, 19, 25]. The creep rate $\dot{\varepsilon}^{\text{vp}}$ in frozen soil is commonly presented as function of time t and not of strain ε^{vp} as in the case of pure ice [22].

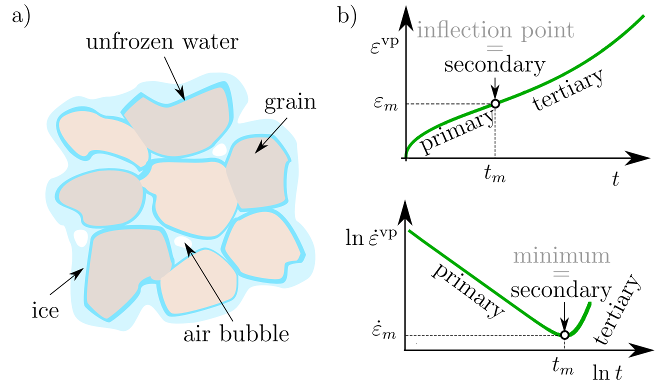

Figure 1: Frozen soil: a) schematic microstructure and b) creep under uniaxial stress $\boldsymbol{\sigma} = \mathrm{diag}(\sigma, 0, 0) = \mathrm{const}$ applied at $t = 0$ with indicated creep stages: strain $\varepsilon^{\mathrm{vp}}$ as function of time t and strain rate $\dot{\varepsilon}^{\mathrm{vp}}$ as function of time t.

2.1. Creep strain ε_m at the slowest creep rate $\dot{\varepsilon}_m$

If a standard (uninterrupted) creep test is conducted under stress $\sigma = \mathrm{const}$ and temperature $\Theta = \mathrm{const}$, the minimum creep rate $\dot{\varepsilon}_m$ is achieved at t_m, see Fig. 1b, after which the creep accelerates. The strain accumulated until t_m,

$$\varepsilon_m = \int_0^{t_m} \dot{\varepsilon}^{\mathrm{vp}} \, \mathrm{d}t = \mathrm{const}\,, \tag{1}$$

turns out to be a material constant [17, 26], i.e., it is independent of σ and Θ. This independence was also observed in the tests reported in Sec. 4.

2.2. Minimum creep rate as a material function $\dot{\varepsilon}_m(\sigma, \Theta)$

Let us now consider two series of standard creep tests, Fig. 2. Tests in the first series differ by the values $\sigma^{(i)}$ of stress and in the second one by the values $\Theta^{(i)}$ [°C] of temperature with $i = 1, 2, 3$. It is evident that the minimum creep rate $\dot{\varepsilon}_m$ increases with σ, see Fig. 2a–b, and with Θ, Fig. 2c–d. Hence, the minimum creep rate $\dot{\varepsilon}_m$ is a function of both, σ and Θ. A possible form of function $\dot{\varepsilon}_m(\sigma, \Theta)$ was defined in [2, 3, 17] and another one in [23].

2.3. Normalised creep curves

Creep curves $\varepsilon^{\mathrm{vp}}(t)$ and $\dot{\varepsilon}^{\mathrm{vp}}(t)$ obtained from experiments, Fig. 2, during a standard (uninterrupted) creep test can be "normalised" as follows: values corresponding to the minimum creep rate: ε_m, $\dot{\varepsilon}_m$ and t_m are used in $\varepsilon^{\mathrm{vp}}/\varepsilon_m(t/t_m)$ and $\dot{\varepsilon}^{\mathrm{vp}}/\dot{\varepsilon}_m(t/t_m)$ as shown in Fig. 3. After such normalisation all experimental curves coincide to a unique curve.

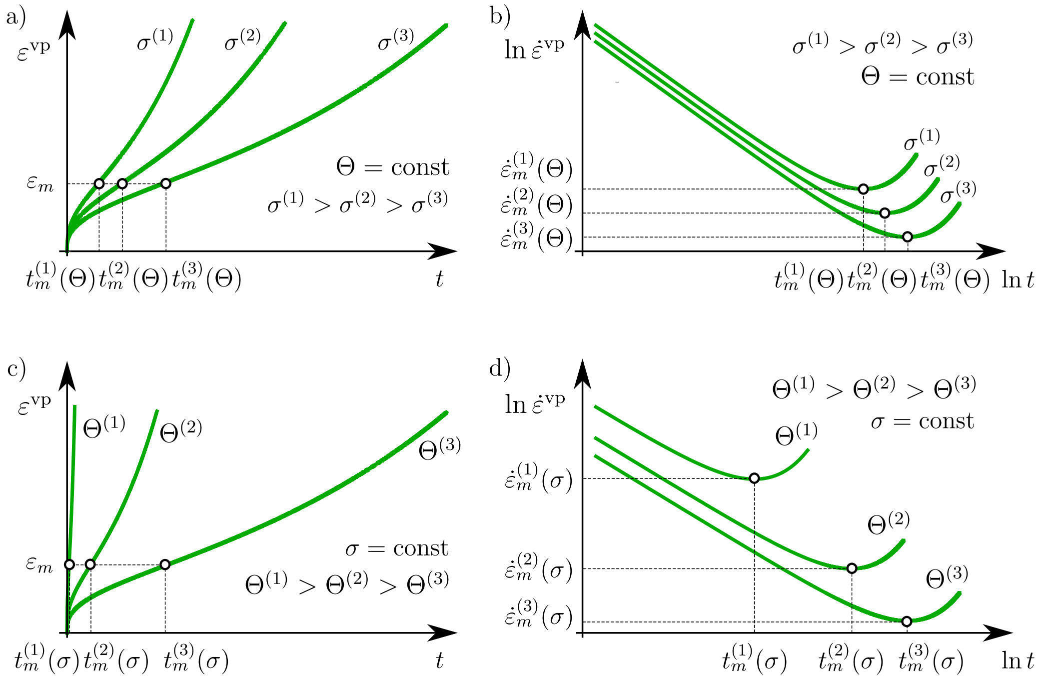

Figure 2: Creep curves in two series of standard creep tests: a) $\varepsilon^{\mathrm{vp}}(t)$ and b) $\dot{\varepsilon}^{\mathrm{vp}}(t)$ in the first series (tests differ by stress σ); c) $\varepsilon^{\mathrm{vp}}(t)$ and d) $\dot{\varepsilon}^{\mathrm{vp}}(t)$ in the second series (tests differ by temperature Θ).

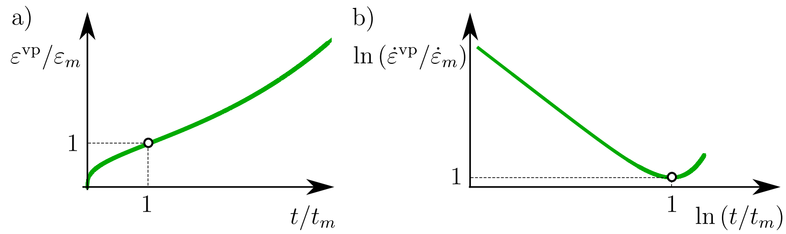

Figure 3: Normalised functions: a) $\varepsilon^{\mathrm{vp}}/\varepsilon_m(t/t_m)$ and b) $\dot{\varepsilon}^{\mathrm{vp}}/\dot{\varepsilon}_m(t/t_m)$.

2.4. Purely volumetric creep

Contrarily to the case of the deviatoric creep, experimental data on the purely volumetric creep of frozen soil can be hardly found in the literature. Several creep tests on frozen sand under isotropic pressure are reported in [4]. Volumetric deformation was measured via the volume change of the cell fluid. The air bubbles in this fluid were not addressed in [4] and hence the results are not reliable. According to the experience made in this study, air bubbles in the cell fluid can strongly influence the measured volumetric strain of the tested samples.

3. Introduction to experiments

Much data on the creep behaviour of frozen sand were provided by Eckardt [5, 6, 7], Orth [17] and Ting [25] in the 80's. Most of these experiments were carried out under uniaxial stress either as constant strain rate (CSR) or as creep tests. A few tests under uniaxial tension [7] and under triaxial stress [17] are also reported. The results from [17] were summarised in the form of several empirical equations describing the creep behaviour of frozen soil depending on the stress level σ and on the temperature Θ. This was a starting point for the constitutive description of the rate-dependent behaviour in frozen soil [2, 3]. Some creep tests with overloadings were conducted in [5]. However, most observations in [17, 25] are applicable to a nearly constant load only. Simulation of creep with interruptions (unloadings, overloadings, reloadings) using the time-based formulations is not possible.

The description of creep proposed in [17] is based on the standing time t_m at $\sigma = \text{const}$ until the minimum creep rate $\dot{\varepsilon}_m$ is reached. Both, t_m and $\dot{\varepsilon}_m$, are measurable. Additional aspects of creep behaviour were investigated under uniaxial stress in this research. These aspects are listed below and described further in Sec. 4.

- Interruptions and recovery of the creep rate

  In order to demonstrate the main shortcoming of the standing time concept, temporary (1 h to 7 days) unloadings of samples were conducted. A variety of further interruptions, i.e., different sets of overloadings and reloadings, allowed an accurate inspection of the creep curves.

- Temperature dependence

  It was essential to investigate how the temperature affects the creep curve.

- Dilatancy and distribution of deformation

  Particle image velocimetry (PIV) technique allowed the measurement of volumetric deformation $\varepsilon^{\mathrm{vp}}_{\mathrm{vol}}$ during creep under uniaxial stress and enabled a better insight into the distribution of deformation within the frozen sample.

- Anisotropy effects

  Anisotropy effects may be very strong in the case of pure ice due to the recrystallization [22]. No experimental evidence could be found in the case of frozen soil. Hence the possible effects of anisotropy were investigated on frozen sand. Before t_m, cubic samples were shortly unloaded, rotated by 90° and then reloaded to study whether such operation can affect the creep rate $\dot{\varepsilon}^{\mathrm{vp}}$.

Additionally, some volumetric creep tests under isotropic compression were conducted in the course of a bachelor thesis at IBF, KIT [35] and their results are summarised in Sec. 5.

- Purely volumetric creep
  Volumetric creep of pure ice under constant isotropic stress is related to the presence of air bubbles in ice [12]. Unfortunately, there is a lack of lab data for frozen soil. Creep tests under isotropic stress are technically troublesome but they confirmed the volumetric creep of frozen soil to be due to the presence of air bubbles only.

Apart from the creep behaviour of artificially frozen sand, other important engineering problems related to frozen soils, like the frost heave in fine-grained soils, have been studied in the literature. The corresponding experimental evidence and constitutive models are reported, for example, in [14, 31, 34].

4. Creep tests under uniaxial compression

Creep tests under uniaxial stress are essential for the formulation of a novel constitutive description. All experiments were conducted in the cold room of the frost laboratory at IBF within a doctoral study and a comprehensive lab report is given in [23]. Stress and temperature levels were chosen in the tests to cover practical values from applications of the ground freezing technology, particularly in tunnel engineering.

4.1. Tested material, sample preparation and experimental procedures

All tests were conducted on Karlsruhe Fine Sand (KFS) which is well-known from numerous works elaborated at IBF, KIT [9, 13, 29, 33]. Basic properties of the tested material are given in Tab. 1.

Two kinds of frozen samples were prepared: conventional cylindrical ones (KS) and cubic ones tested either without (A) or with the PIV (AF). Cylindrical samples had the diameter of 10 cm and the height of 15.5 cm. Samples for testing of anisotropy were chosen to have the cubic

Table 1: Basic properties of Karlsruhe Fine Sand (KFS).

d_{50}	C_u	ρ_s	$e_{\max}$	$e_{\min}$	φ
mm	-	g/cm^3	-	-	$\circ$
0.14	1.5	2.65	1.054	0.677	33.1

form. Such form also facilitated the processing of data in the case of tests with the PIV. Size of the cubes was constrained by the available freezing equipment to $7 \times 7 \times 7$ cm^3.

Sample preparation was aimed at the reproducibility, full saturation and homogeneity of porosity. Void ratio e, degree of saturation S and density index I_D of all samples referred in this paper are given in Tab. 2.

Table 2: Void ratio e, density index I_D and degree of saturation S: cylindrical samples (KS), cubic samples (A) and cubic samples tested with the PIV (AF).

Sample	S	e	I_D
	-	-	-
KS1	0.95	0.88	0.47
KS2	0.99	0.84	0.58
KS3	1.00	0.85	0.55
KS4	0.97	0.87	0.48
KS7	0.97	0.72	0.89
KS8	0.98	0.70	0.94
KS9	0.98	0.71	0.91
KS10	0.99	0.73	0.87
KS11	0.98	0.71	0.91
A1[a]	-	0.73	0.87
A2[a]	-	0.72	0.89
A3	0.97	0.72	0.89
A5	0.96	0.73	0.85
A6	0.96	0.72	0.90
A7	0.96	0.72	0.88
A8	0.95	0.72	0.89
AF1	0.93	0.77	0.76
AF2	0.95	0.76	0.79
AF5	0.96	0.74	0.83
AF6	0.96	0.76	0.79
AF7	0.96	0.76	0.79
AF8	0.96	0.74	0.84
AF9	0.96	0.76	0.78
AF10	0.96	0.76	0.78
AF11	0.95	0.76	0.78
AF12	0.95	0.79	0.71
AF13	0.95	0.73	0.85
AF14	0.96	0.75	0.81
AF15	0.92	0.76	0.79
AF16	0.96	0.73	0.85
AF17	0.97	0.75	0.82

[a] Dry mass of the sample was not measured after the test.

4.2. Processing of data

Data acquisition was done by the data logger of the hydraulic press. For the postprocessing, a self-developed MATHEMATICA [30] package `Freeze‘` was used. The scatter in results (creep strain and its rate) was smoothed using a Gaussian kernel and the results were plotted in the form of creep curves. Gaussian kernel with the radius r was applied and the smoothing caused the loss of r first and r last measurements in each list of results. This can be seen in the reported diagrams, e.g., the plotted $\dot{\varepsilon}^{\text{vp}}(\varepsilon^{\text{vp}})$ curves do not start at $\varepsilon^{\text{vp}} = 0$.

Greased rubber pads were placed at the interfaces between the sample and the end plates of the testing device to reduce friction and to improve the uniformity of stress distribution within the sample. However, the strain measured via the displacement of the end plate during the test includes a portion from the rubber pads with grease. The part of deformation resulting from compression of these pads is called the *bedding error*. It was measured and taken into account in the processing of data [23].

4.3. Interruptions and recovery of the creep rate

From the practical point of view, a constitutive description should consider a general case of creep interrupted by different sets of unloadings, overloadings, reloadings. For this purpose, the existence of a unique creep curve $\dot{\varepsilon}^{\text{vp}}/\dot{\varepsilon}_m(\varepsilon^{\text{vp}}/\varepsilon_m)$ specific to a given type of frozen soil is postulated. This *universal creep curve* was verified by conduction of the tests with different interruptions.

4.3.1. Standard (uninterrupted) creep tests (C)

To examine whether the interruptions affect the creep rate, the referential standard creep test (C) will be used for comparison. 14 such C tests were carried out under various conditions. Details on these tests are included in Tab. 3.

Note that the representation $\dot{\varepsilon}^{\text{vp}}(\varepsilon^{\text{vp}})$ is common in the glaciological literature, e.g., [22]. The advantage of $\dot{\varepsilon}^{\text{vp}}(\varepsilon^{\text{vp}})$ over $\dot{\varepsilon}^{\text{vp}}(t)$ is due to the autonomy of $\dot{\varepsilon}^{\text{vp}}(\varepsilon^{\text{vp}})$. Hence, the creep rates from all C tests are shown in Fig. 4 in the form of $\dot{\varepsilon}^{\text{vp}}(\varepsilon^{\text{vp}})$ graphs.

Unfortunately, a considerable scatter of the test results can be seen in Fig. 4. No systematic relation of this scatter to discrepancies in the physical parameters of the samples, like the void ratio e, could be recognised. This scatter can be a consequence of the used lab technique. The novel preparation technique might have caused the heterogeneity of samples. Influence of

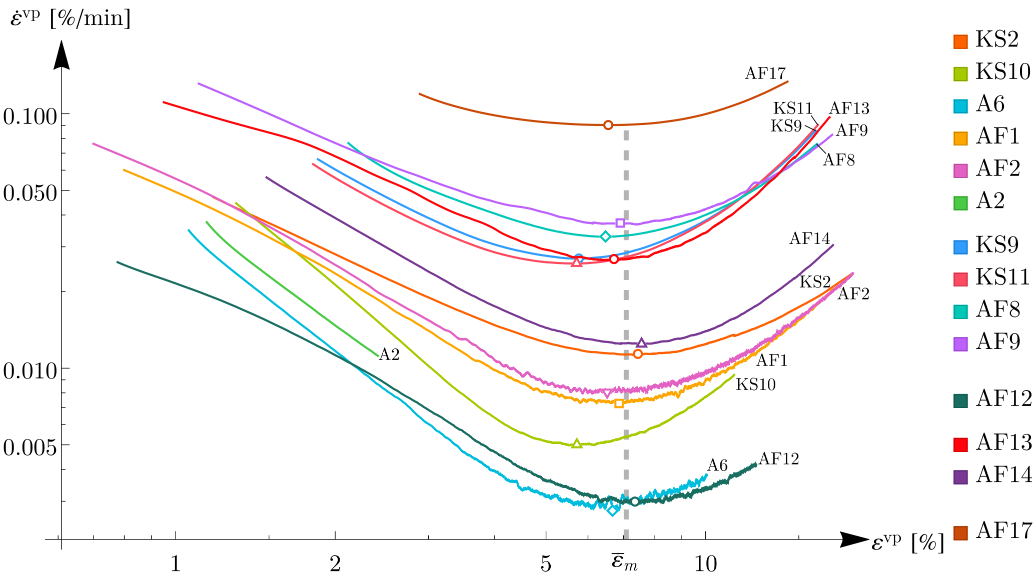

Figure 4: $\dot{\varepsilon}^{vp}(\varepsilon^{vp})$ curves in all C tests at various σ and Θ with indicated minima $(\varepsilon_m, \dot{\varepsilon}_m)$.

different lab techniques (like air-pluviation, water-pluviation) on the scatter in results should be conducted. The problem of the scatter in results of experiments on frozen soils is addressed, e.g., in [15].

Table 3: Summary of C tests.

Sample/ Test	Type of test	Θ °C	σ MPa	t_m min	ε_m %	$\dot{\varepsilon}_m$ %/min
KS2	C	-10	5	431.0	7.5	$1.1 \cdot 10^{-2}$
KS9	C	-10	7	136.1	5.8	$2.7 \cdot 10^{-2}$
KS10	C	-10	5	544.5	5.7	$5.0 \cdot 10^{-3}$
KS11	C	-10	7	142.4	5.7	$2.6 \cdot 10^{-2}$
A2[a]	C	-10	5	-	-	-
A6[b]	C	-10	5	1241.6	6.7	$2.8 \cdot 10^{-3}$
AF1	C	-10	5	545.3	6.9	$7.3 \cdot 10^{-3}$
AF2	C	-10	5	452.1	6.5	$8.0 \cdot 10^{-3}$
AF8	C	-10	7	127.9	6.5	$3.3 \cdot 10^{-2}$
AF9	C	-10	7	124.4	6.9	$3.7 \cdot 10^{-2}$
AF12	C	-20	7	1375.6	7.4	$3.0 \cdot 10^{-3}$
AF13	C	-15	7	156.2	6.7	$2.7 \cdot 10^{-2}$
AF14	C	-15	7	376.2	7.6	$1.2 \cdot 10^{-2}$
AF17	C	-5	4	57.4	6.6	$9.0 \cdot 10^{-2}$

[a] Sample was pressed out of the testing device during the primary creep due to a geometrical irregularity in the testing device.

[b] Sample demonstrated an anomalous behaviour.

4.3.2. *Creep tests with an unloading-reloading cycle (CurC)*

The main shortcoming of $\dot{\varepsilon}^{\mathrm{vp}}(t)$ concept can be easily demonstrated by the creep test interrupted by a temporary unloading followed by reloading. The sample regains its previous rate of creep and this contradicts the direct dependence $\dot{\varepsilon}^{\mathrm{vp}}(t)$.

4 tests with an unloading-reloading cycle (CurC) were carried out at $\sigma = 5$ MPa and $\Theta = -10$ °C, see Tab. 4. During the primary creep, the samples were temporarily unloaded at $t = 20\%..30\%\,\bar{t}_m$. Mean value of the standing time $\bar{t}_m$ is known from the referential C tests from Tab. 3. Samples were quickly unloaded from $\sigma = 5$ MPa to $\sigma = 0.1..0.2$ MPa (= the weight of piston in the testing device).

The durations of pauses were: 1 h, 24 h, 24 h and 7 days in the case of samples: AF6, AF10, AF11 and AF15, respectively. After the interruption period (pause), the samples were reloaded back to $\sigma = 5$ MPa and the creep rate prior to the unloading was regained. Creep curves $\varepsilon^{\mathrm{vp}}(t)$ can be recovered after a time shift-back corresponding to the duration of the interruption, see Fig. 5a–b. Creep rates $\dot{\varepsilon}^{\mathrm{vp}}(\varepsilon^{\mathrm{vp}})$ were obtained using the shifted curves $\varepsilon^{\mathrm{vp}}(t)$ from all CurC tests and are plotted in Fig. 6. Recovery of the creep rate after the unloading period is evident.

No influence of the interruptions on the minimum creep rate $\dot{\varepsilon}_m$ can be infered from comparison with 4 corresponding C tests from Fig. 4. Creep curves $\dot{\varepsilon}^{\mathrm{vp}}(\varepsilon^{\mathrm{vp}})$ from all CurC tests are shown together with the ones from the 4 referential C tests in Fig. 7. It follows from Fig. 7 that the results from CurC tests lie within the experimental scatter obtained from the C tests. No systematic influence of the duration of the unloading can be concluded.

Table 4: Summary of CurC tests and referential C tests (excluding failed test A2 and anomalous test A6).

Sample/ Test	Type of test	Θ °C	σ MPa	ε_m %	$\dot{\varepsilon}_m$ %/min
KS2	C (ref.)	−10	5	7.5	$1.1 \cdot 10^{-2}$
KS10	C (ref.)	−10	5	5.7	$5.0 \cdot 10^{-3}$
AF1	C (ref.)	−10	5	6.9	$7.3 \cdot 10^{-3}$
AF2	C (ref.)	−10	5	6.5	$8.0 \cdot 10^{-3}$
AF6	CurC(1 h)	−10	5	7.3	$6.2 \cdot 10^{-3}$
AF10	CurC(24 h)	−10	5	7.2	$9.5 \cdot 10^{-3}$
AF11	CurC(24 h)	−10	5	7.5	$1.1 \cdot 10^{-2}$
AF15	CurC(7 days)	−10	5	7.4	$1.5 \cdot 10^{-2}$

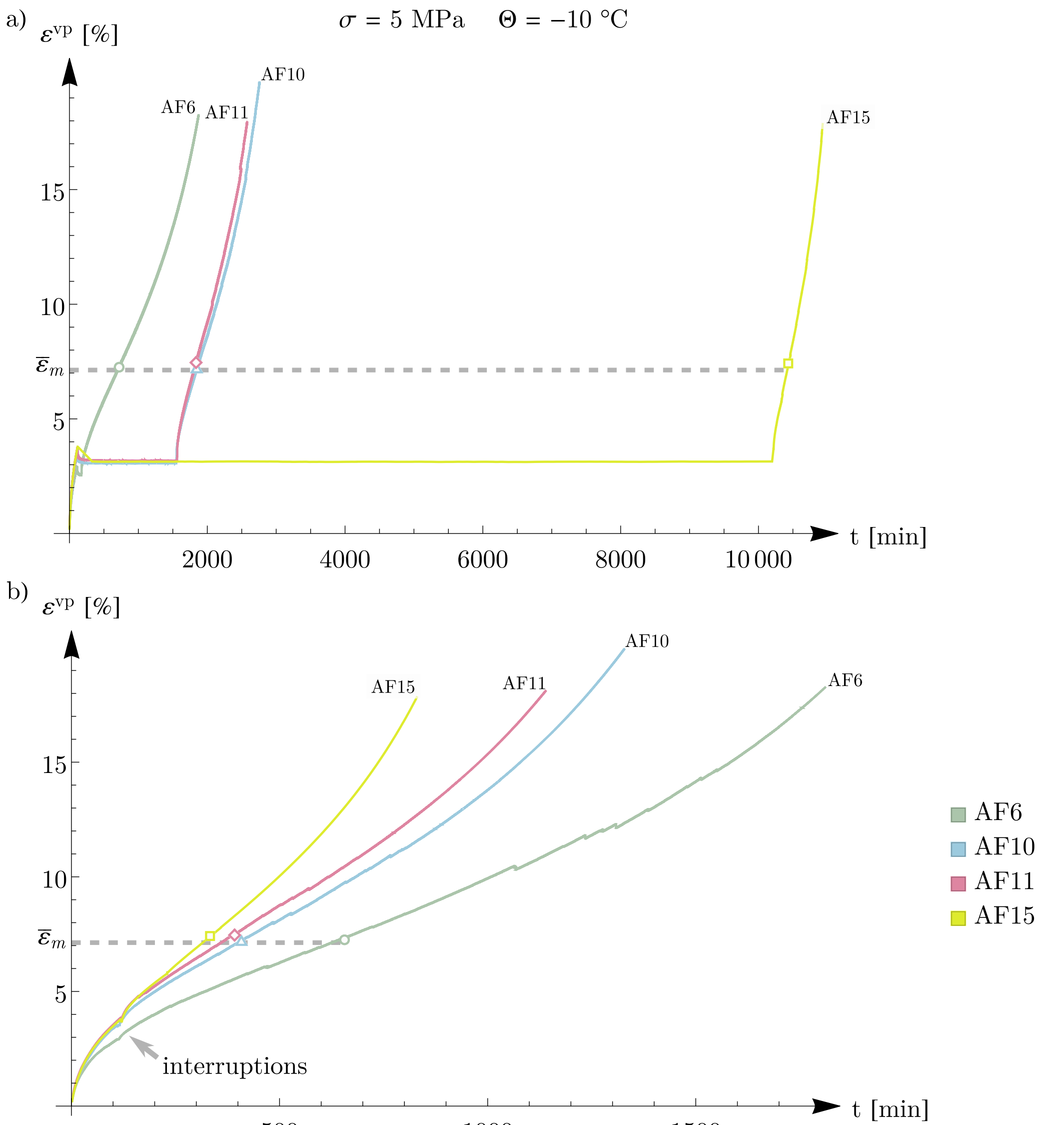

Figure 5: $\varepsilon^{\mathrm{vp}}(t)$ curves in CurC tests with indicated inflections ("t_m", ε_m) (Standing time has no meaning and hence is denoted as "t_m".): a) unloading periods are included; b) curves are shifted back in time by duration of unloading.

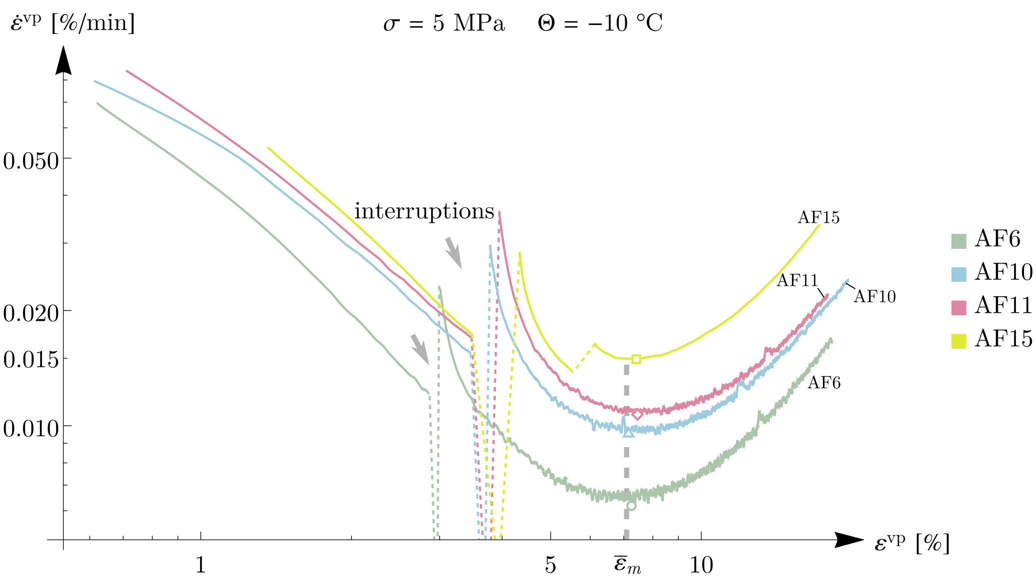

Figure 6: $\dot{\varepsilon}^{vp}(\varepsilon^{vp})$ curves in CurC tests with indicated minima $(\varepsilon_m, \dot{\varepsilon}_m)$. An additional interruption can be seen in test AF15 after reloading. It is due to a failure in the control system.

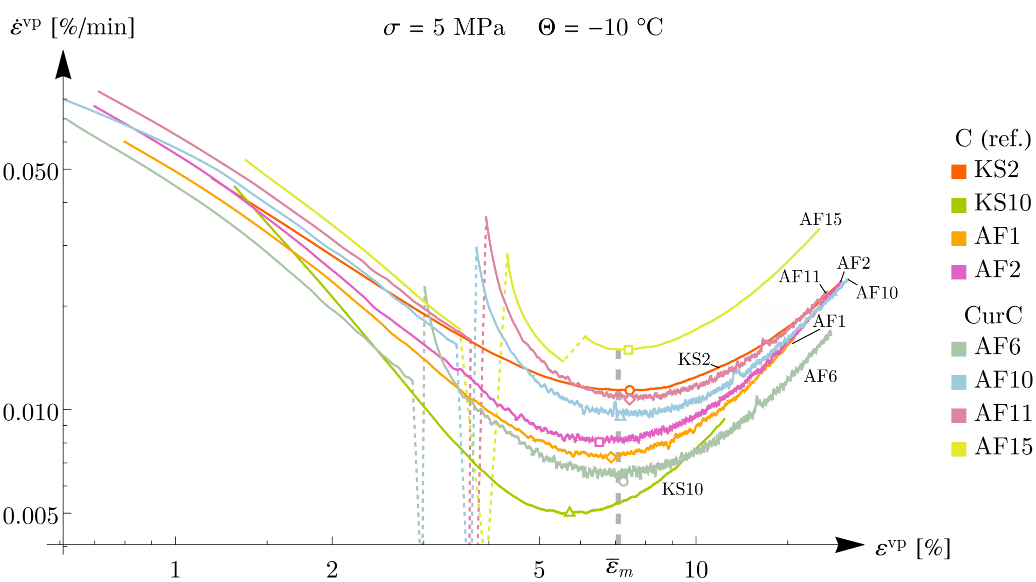

Figure 7: $\dot{\varepsilon}^{vp}(\varepsilon^{vp})$ curves in CurC tests and referential C tests with indicated minima $(\varepsilon_m, \dot{\varepsilon}_m)$.

4.3.3. Creep tests with overloadings/reloadings (CoC and CoCrC)

Creep curve was also tested with other interruptions. Two types of creep tests with overloadings/reloadings were carried out on 6 samples at $\Theta = -10$ °C, see Tab. 5. Before the slowest creep rate was achieved, samples from the first group (CoC) were only overloaded. They reached $\dot{\varepsilon}_m$ under such increased stress. Samples in CoCrC tests were at first overloaded and then reloaded back to the previous stress. Hence, the minimum creep rate was obtained under the initial load.

Similarly to the CurC tests, creep of all (but KS1) samples was interrupted at $t = 20\%..30\%\,\bar{t}_m$. Mean value of the standing time $\bar{t}_m$ could be determined basing on the referential C tests, see Tab. 3. Samples from the second group (CoCrC) were unloaded to the initial stress after 20..30 min of the overloading.

KS1 was the first tested sample. It was meant to be a C test under $\sigma = 3.5$ MPa but the minimum rate was not achieved at the expected time. Hence the sample was gradually overloaded. For this reason KS1 is counted among the CoC tests.

Creep curves $\varepsilon^{\mathrm{vp}}(t)$ from all CoC and CoCrC tests are given in Fig. 8. Interpretation of the results is now somewhat more complicated than previously, in CurC tests. In the case of CoC tests, the initial $\sigma = 5$ MPa leaves a considerable creep deformation. In CoCrC tests, also a significant creep strain is accumulated under the overload.

The regained (after reloading) part of $\varepsilon^{\mathrm{vp}}(t)$ from a CoCrC test could be possibly shifted forward in time until it meets the referential curve at the same creep strain. However, this only confirms the invalidity of time as an argument in the creep rate function. A general description of the creep behaviour basing on the time representation in the case of overloading is impossible.

Summing up, no clear conclusions can be drawn about the influence of overloadings/reloadings on the creep curve judging by $\varepsilon^{\mathrm{vp}}(t)$. However, curves $\dot{\varepsilon}^{\mathrm{vp}}(\varepsilon^{\mathrm{vp}})$ can be at least directly compared. Time-dependent description $\dot{\varepsilon}^{\mathrm{vp}}(t)$ cannot be generalised. Creep rates from the CoC and CoCrC tests are given in Fig. 9 seperately depending on stress σ at which the tertiary creep was approached. These curves are additionally plotted together with the referential C tests in Fig. 10.

It can be seen in Fig. 9a that the behaviour of sample KS7 stands a bit aside from the others because KS7 achieved quite slower $\dot{\varepsilon}_m$. However, this deviation seems to be within the experimental scatter as shown in Fig. 10a. Apart from that, the target creep curve $\dot{\varepsilon}^{\mathrm{vp}}(\varepsilon^{\mathrm{vp}})$ is always regained, see Fig. 10a–b. Neither the minimum rate $\dot{\varepsilon}_m$ is pronouncably affected by the overloadings/reloadings.

Additionally, the creep rate $\dot{\varepsilon}^{\mathrm{vp}}(\varepsilon^{\mathrm{vp}})$ is plotted for CoCrC tests and the referential C tests at both, $\sigma = 5$ MPa and $\sigma = 7$ MPa, Fig. 11. It can be observed how $\dot{\varepsilon}^{\mathrm{vp}}$ switches between the creep isobars depending on the current stress level.

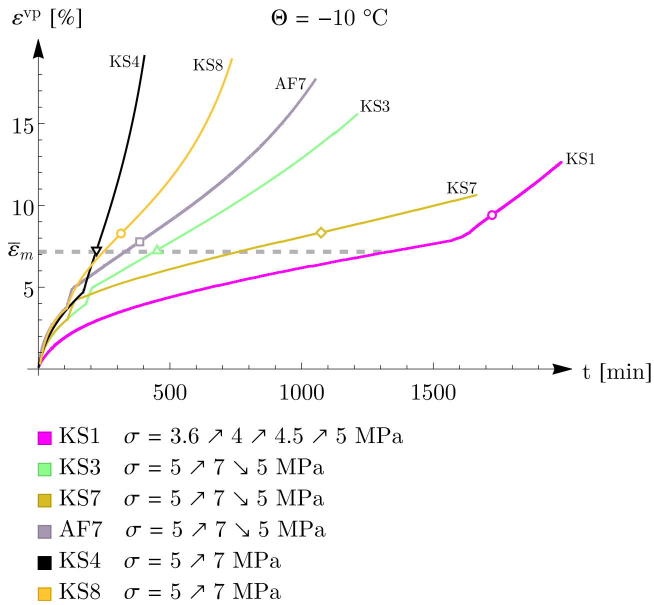

Figure 8: $\varepsilon^{\mathrm{vp}}(t)$ curves in CoC and CoCrC tests with indicated inflections ("t_m", ε_m). (Standing time has no meaning and hence is denoted as "t_m".)

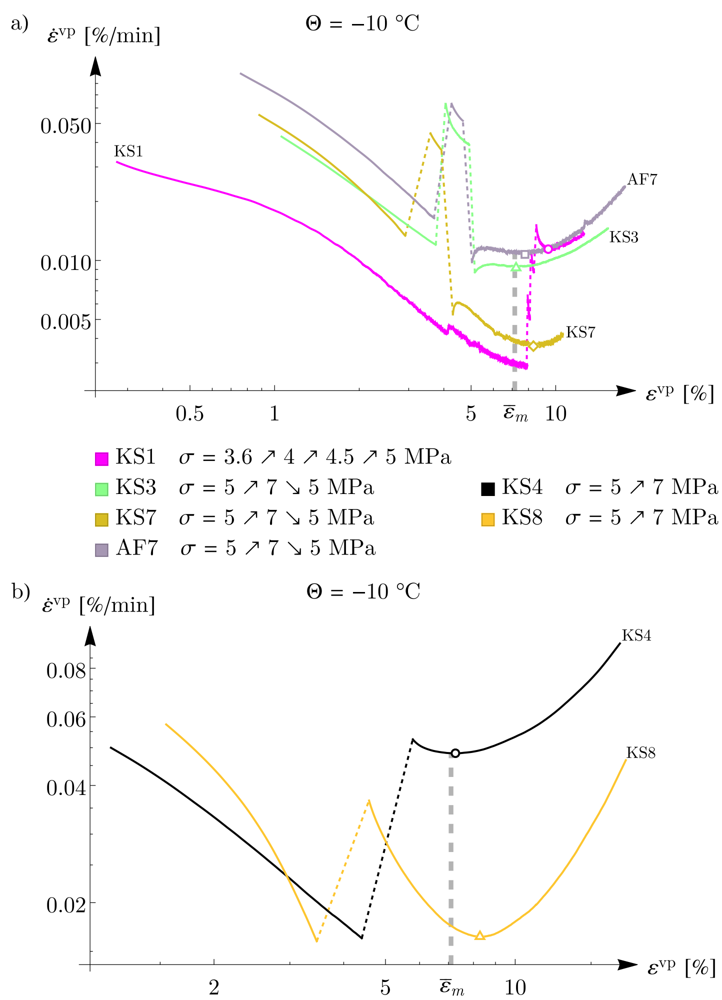

Figure 9: CoC and CoCrC tests with indicated minima $(\varepsilon_m, \dot{\varepsilon}_m)$: a) $\dot{\varepsilon}^{\mathrm{vp}}(\varepsilon^{\mathrm{vp}})$ curves in CoC and CoCrC tests in which $\dot{\varepsilon}_m$ was achieved at $\sigma = 5$ MPa; b) $\dot{\varepsilon}^{\mathrm{vp}}(\varepsilon^{\mathrm{vp}})$ curves in CoC tests in which $\dot{\varepsilon}_m$ was achieved at $\sigma = 7$ MPa.

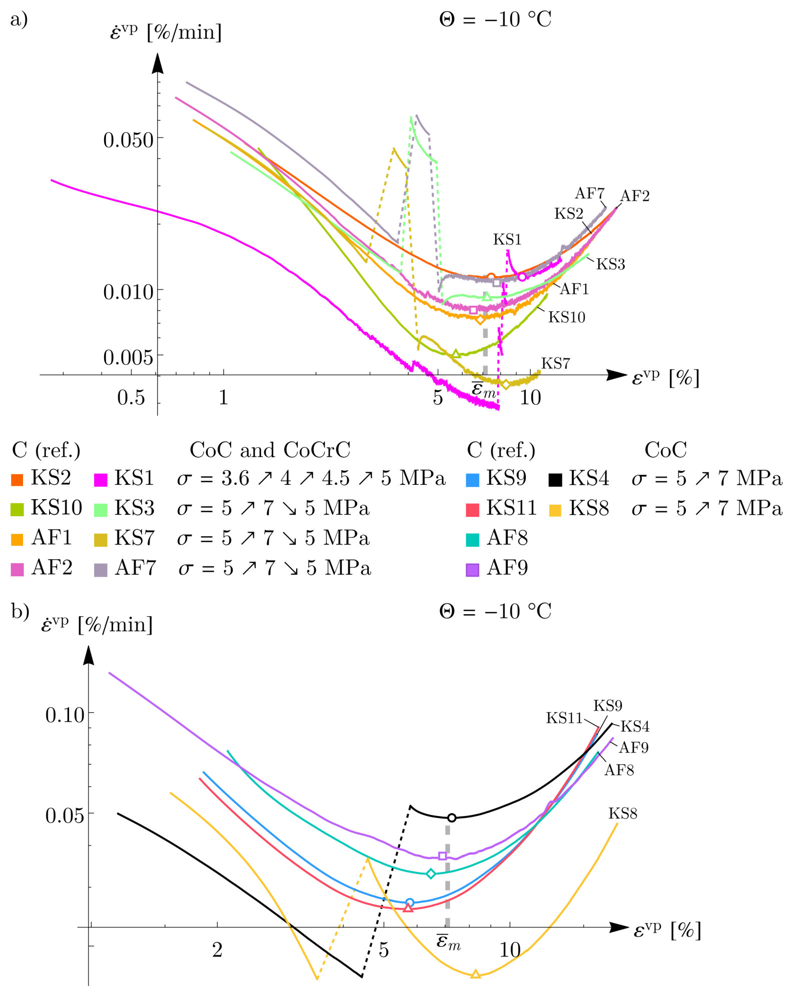

Figure 10: CoC and CoCrC tests and referential C tests with indicated minima $(\varepsilon_m, \dot{\varepsilon}_m)$: a) $\dot{\varepsilon}^{\mathrm{vp}}(\varepsilon^{\mathrm{vp}})$ curves in CoC, CoCrC and C tests in which $\dot{\varepsilon}_m$ was achieved at $\sigma = 5$ MPa; b) $\dot{\varepsilon}^{\mathrm{vp}}(\varepsilon^{\mathrm{vp}})$ curves in CoC and C tests in which $\dot{\varepsilon}_m$ was achieved at $\sigma = 7$ MPa.

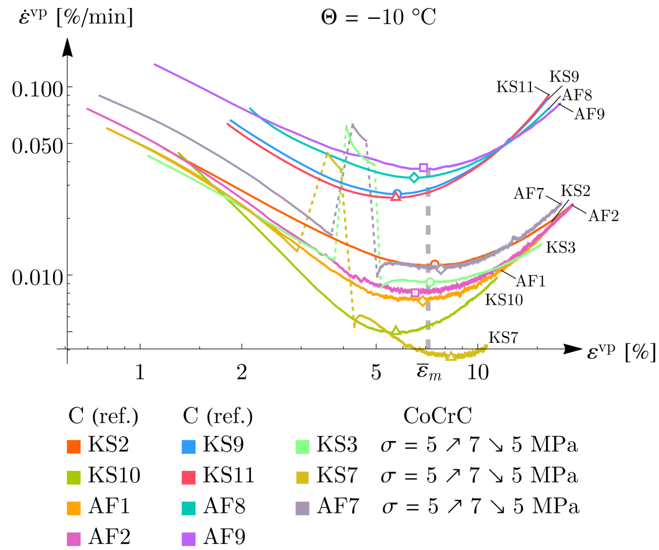

Figure 11: $\dot{\varepsilon}^{\mathrm{vp}}(\varepsilon^{\mathrm{vp}})$ curves in CoCrC tests and referential C tests at both, $\sigma = 5$ MPa and $\sigma = 7$ MPa, with indicated minima $(\varepsilon_m, \dot{\varepsilon}_m)$.

Table 5: Summary of CoC and CoCrC tests and referential C tests (excluding failed test A2 and anomalous test A6).

Sample/ Test	Type of test	Θ °C	σ MPa	ε_m %	$\dot{\varepsilon}_m$ %/min
KS2	C (ref.)	−10	5	7.5	$1.1 \cdot 10^{-2}$
KS9	C (ref.)	−10	7	5.8	$2.7 \cdot 10^{-2}$
KS10	C (ref.)	−10	5	5.7	$5.0 \cdot 10^{-3}$
KS11	C (ref.)	−10	7	5.7	$2.6 \cdot 10^{-2}$
AF1	C (ref.)	−10	5	6.9	$7.3 \cdot 10^{-3}$
AF2	C (ref.)	−10	5	6.5	$8.0 \cdot 10^{-3}$
AF8	C (ref.)	−10	7	6.5	$3.3 \cdot 10^{-2}$
AF9	C (ref.)	−10	7	6.9	$3.7 \cdot 10^{-2}$
KS1	CoC	−10	$3.6 \nearrow 4 \nearrow 4.5 \nearrow 5$	9.4	$1.1 \cdot 10^{-2}$
KS3	CoCrC	−10	$5 \nearrow 7 \searrow 5$	7.2	$9.2 \cdot 10^{-3}$
KS4	CoC	−10	$5 \nearrow 7$	7.3	$4.8 \cdot 10^{-2}$
KS7	CoCrC	−10	$5 \nearrow 7 \searrow 5$	8.3	$3.6 \cdot 10^{-3}$
KS8	CoC	−10	$5 \nearrow 7$	8.3	$1.6 \cdot 10^{-2}$
AF7	CoCrC	−10	$5 \nearrow 7 \searrow 5$	7.8	$1.1 \cdot 10^{-2}$

4.3.4. *Creep strain ε_m at the slowest creep rate $\dot{\varepsilon}_m$*

The strain ε^{vp} is understood as the creep deformation measured from the configuration at which the sample was frozen. The irreversible strain ε_m is defined as 1D ε^{vp} accumulated until the slowest creep rate $\dot{\varepsilon}_m$ is achieved. This ε_m is used in the literature as a material constant, see Sec. 2. This parameter can be evaluated for frozen KFS from all creep curves in Secs. 4.3.1–4.3.3. The values of ε_m from all tests on frozen KFS are presented in Fig. 12.

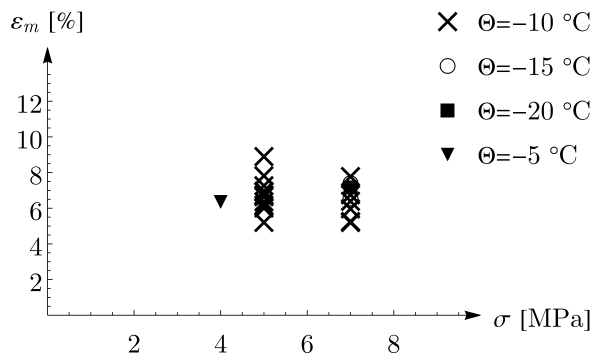

Figure 12: Creep strain ε_m accumulated until the slowest creep rate $\dot{\varepsilon}_m$ as obtained from all C, CurC, CoC and CoCrC tests.

Apart from some scatter, a nearly constant (independent of σ and Θ) value of ε_m can be concluded from Fig. 12. The scatter of ε_m may follow from inaccuracies in manual measurement of the sample height. Mean value $\bar{\varepsilon}_m = 7.1\%$ was found with the standard deviation of 0.9%.

4.3.5. *Minimum creep rate as a material function $\dot{\varepsilon}_m(\sigma, \Theta)$*

The slowest creep rate $\dot{\varepsilon}_m$ in all C, CurC, CoC and CoCrC tests can be found in Fig. 13. The function $\dot{\varepsilon}_m(\sigma, \Theta)$ can be obtained as, e.g., the inverted $\sigma = \sigma_\alpha + c(\Theta) \ln(\dot{\varepsilon}_m/\dot{\varepsilon}_\alpha)$, with the reference values σ_α and $\dot{\varepsilon}_\alpha$ [2, 3, 17].

4.3.6. *Universal creep curve $\dot{\varepsilon}^{vp}/\dot{\varepsilon}_m(\varepsilon^{vp}/\varepsilon_m)$*

Creep curves obtained from standard (uninterrupted) tests and “normalised” in the time representation $\dot{\varepsilon}^{\text{vp}}/\dot{\varepsilon}_m(t/t_m)$ are well-known in the literature, see Sec. 2. Analogous normalisation can be used for curves $\dot{\varepsilon}^{\text{vp}}(\varepsilon^{\text{vp}})$, that is, $\dot{\varepsilon}^{\text{vp}}/\dot{\varepsilon}_m(\varepsilon^{\text{vp}}/\varepsilon_m)$. In this way, one can normalise also the results from tests with interruptions.

This normalised representation is called the *universal creep curve* here. It is postulated to be specific to a given type of frozen soil. Normalised curves $\dot{\varepsilon}^{\text{vp}}/\dot{\varepsilon}_m(\varepsilon^{\text{vp}}/\varepsilon_m)$ from all experiments

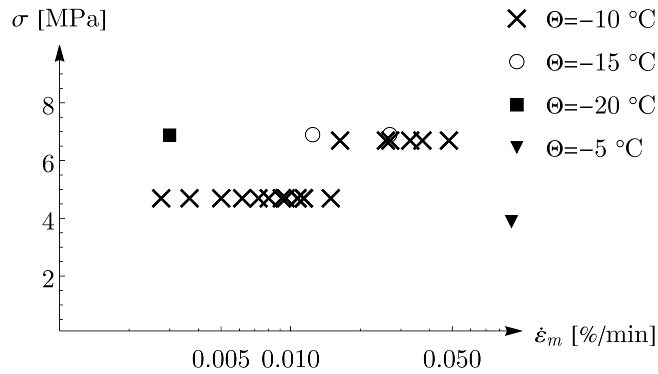

Figure 13: Creep stress σ as function of minimum creep rate $\dot{\varepsilon}_m$ at different temperatures Θ as obtained from all C, CurC, CoC and CoCrC tests.

reported in Secs. 4.3.1–4.3.3 are shown in Fig. 14. These curves coincide quite well which justifies the term *universal* creep curve for frozen KFS.

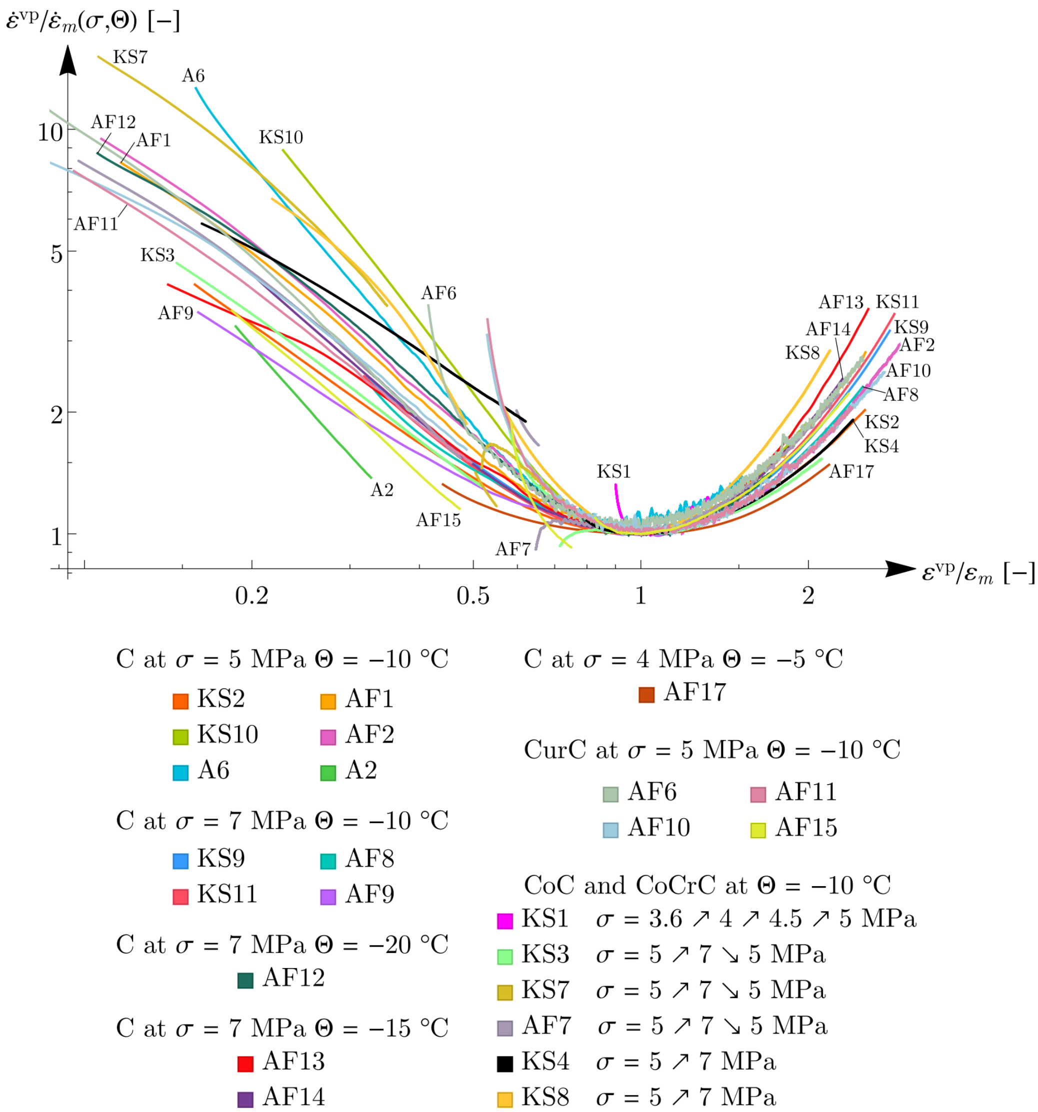

Figure 14: Normalised creep curves $\dot{\varepsilon}^{\mathrm{vp}}/\dot{\varepsilon}_m(\varepsilon^{\mathrm{vp}}/\varepsilon_m)$ from all C, CurC, CoC and CoCrC tests on frozen KFS.

4.4. Dilatancy and distribution of deformation

During creep tests on frozen soil under uniaxial compression, volume changes $\dot{V} \neq 0$ of the sample are commonly disregarded [17]. One believes that the samples are perfectly saturated and the substance (ice + soil particles) is volumetrically incompressible. Moreover, there are technical difficulties in the measurement of the volume change. In the course of this research, measurement of the volume change was undertaken and a significant volumetric creep deformation of the sample could be concluded.

To overcome complications involved in the local (contact) measurement of the horizontal displacement of the sample, one can invoke the image-based techniques, like the PIV [1, 21, 27, 28, 32]. It stems from fluid mechanics and allows the measurement of the displacement or velocity field of a substance. In particular, the PIV can be used to measure deformation of a frozen soil sample during creep. Given two 2D displacement fields on two perpendicular faces of a cubic sample, the volume change can be determined. Not only the average deformation but also the *distribution* of deformation can be obtained for the faces of the sample.

Experimental data from the PIV were obtained in the form of series of images from two cameras, one per face. The images were processed on a PC using a self-developed Mathematica package `flowTrack`` to find the deformation field. The Mathematica internal procedure `ImageDisplacements[]` was used. It estimates the displacement field between two subsequent images for each pixel based on the so-called *dense optical flow* [10, 21]. Displacement fields between the subsequent images were obtained in the spatial description and needed to be integrated into the material description for a whole series of images. The results obtained from the PIV were processed and plotted in the form of displacement fields and strain fields [23].

4.4.1. Volumetric strain ε_{vol}^{vp}

Dilatancy (or contractancy) was investigated on frozen sand samples during creep under uniaxial stress. The PIV provided a supplementary measurement of the average vertical strain but it was essential for the average horizontal strain. It was measured for two walls of the cubic sample as $\varepsilon_{11}^{\mathrm{vp}}$ and $\varepsilon_{22}^{\mathrm{vp}}$, Fig. 15. In this way, the volumetric deformation $\varepsilon_{\mathrm{vol}}^{\mathrm{vp}}$ could be determined.

10 creep tests on the cubic samples (AF) from Sec. 4.3 that were conducted with the PIV are listed in Tab. 6. Usable results from the PIV could not always be obtained for the whole test. This was predominantly due to the so-called pixel renegades, i.e., the particles falling down

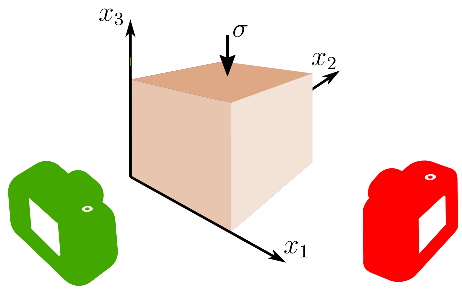

Figure 15: Cartesian coordinate system for frozen sample during creep under uniaxial stress in tests with the PIV with two cameras.

from the sample face. This problem aggregates with increasing deformation of the sample. 294
The average horizontal strain $\varepsilon^{\rm vp}_{\rm hor}$ obtained for both walls of the sample (as $\varepsilon^{\rm vp}_{11}$ and $\varepsilon^{\rm vp}_{22}$) is given 295
in Fig. 16 as a function of the average vertical strain, $\varepsilon^{\rm vp} \equiv \varepsilon^{\rm vp}_{\rm vert}$ (measured as $\varepsilon^{\rm vp}_{33}$). In the case 296
of samples AF9 and AF13, $\varepsilon^{\rm vp}_{\rm hor}$ could be obtained from the PIV on one wall only and the same 297
$\varepsilon^{\rm vp}_{\rm hor}$ was assumed for the second wall in calculation of $\varepsilon^{\rm vp}_{\rm vol}$ $(=\varepsilon^{\rm vp}_{11} + \varepsilon^{\rm vp}_{22} + \varepsilon^{\rm vp}_{33})$. 298
It can be seen in Fig. 16 that the measurements of the horizontal strain $\varepsilon^{\rm vp}_{\rm hor}$ from all tests 299
coincide almost perfectly, independently of the testing conditions, σ and Θ. The only exception 300
is $\varepsilon^{\rm vp}_{\rm hor}$ measured on one face of sample AF7 and the most probable reason of this deviation are 301
the pixel renegades. 302
Despite the scatter (due to the used lab technique), it can be concluded from $\varepsilon^{\rm vp}_{\rm vol}(\varepsilon^{\rm vp}_{\rm vert})$ plots 303
given in Fig. 17 that in the primary creep stage the samples undergo initially the contractancy, 304
$\dot{\varepsilon}^{\rm vp}_{\rm vol} > 0$. The dilatancy takes over roughly at $\varepsilon^{\rm vp}_{\rm vert} = \frac{1}{2}\varepsilon_m$ and the accumulated compressive 305
volumetric strain $\varepsilon^{\rm vp}_{\rm vol} > 0$ starts being reduced. The excess of the sample volume over the initial 306
value, described by $\varepsilon^{\rm vp}_{\rm vol} < 0$, clearly marks the beginning of the tertiary stage. 307
The contractancy/dilatancy is most likely related to the compression/expansion of air bubbles 308
in ice. This can be accompanied by the dissolution/nucleation and diffusion of bubbles. The 309
dilatancy at $\varepsilon^{\rm vp}_{\rm vol} < 0$ is probably caused by the development and propagation of cracks within 310
the sample. 311

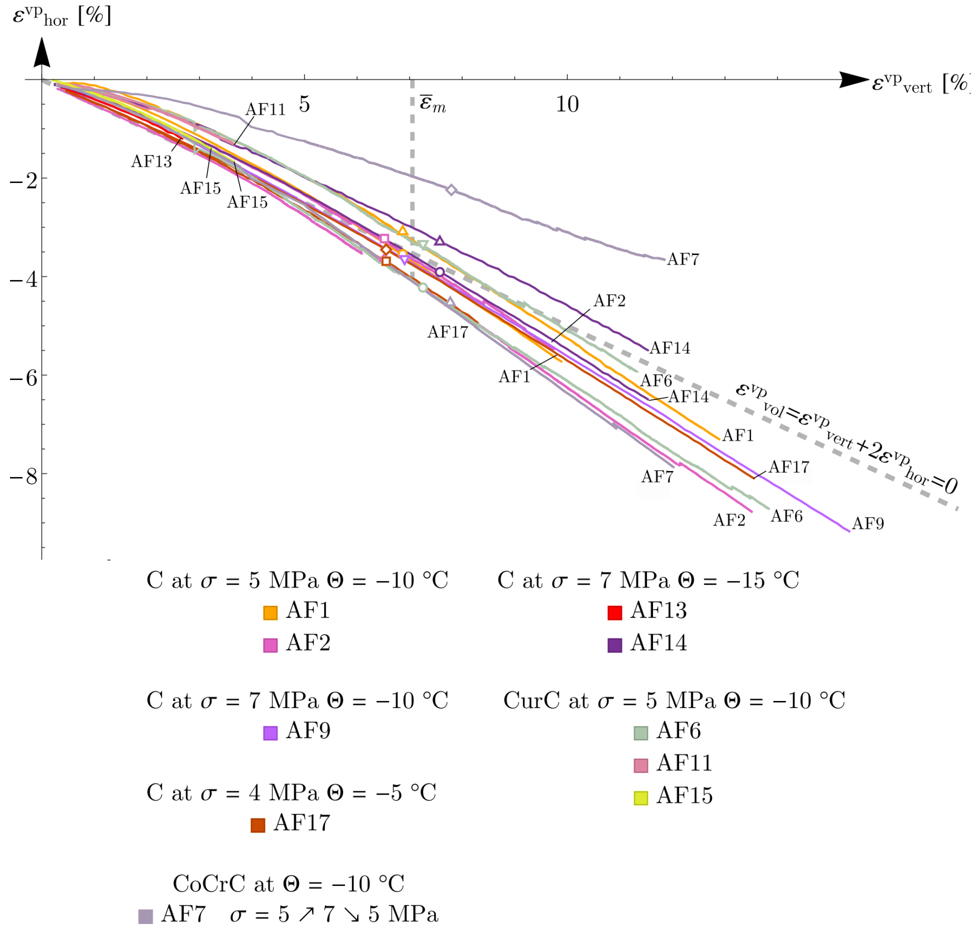

Figure 16: $\varepsilon^{vp}_{hor}(\varepsilon^{vp}_{vert})$ curves in C, CurC, CoCrC tests with indicated pairs $(\varepsilon_m, \varepsilon^{vp}_{hor}(\varepsilon_m))$ at $\dot{\varepsilon}_m$.

Table 6: Summary of C, CurC and CoCrC tests extended with the PIV results.

Sample/ Test	Type of test	Θ °C	σ MPa	ε_m %	$\dot{\varepsilon}_m$ %/min	$\varepsilon^{vp}_{vol}(\varepsilon_m)$ %
AF1	C	−10	5	6.9	$7.3 \cdot 10^{-3}$	0.2
AF2	C	−10	5	6.5	$8.0 \cdot 10^{-3}$	-0.4
AF9	C	−10	7	6.9	$3.7 \cdot 10^{-2}$	-0.4
AF13	C	−15	7	6.7	$2.7 \cdot 10^{-2}$	-
AF14	C	−15	7	7.6	$1.2 \cdot 10^{-2}$	0.4
AF17	C	−5	4	6.6	$9.0 \cdot 10^{-2}$	-0.6
AF6	CurC(1 h)	−10	5	7.3	$6.2 \cdot 10^{-3}$	-0.3
AF11	CurC(24 h)	−10	5	7.5	$1.1 \cdot 10^{-2}$	-
AF15	CurC(7 days)	−10	5	7.4	$1.5 \cdot 10^{-2}$	-
AF7	CoCrC	−10	5 ↗ 7 ↘ 5	7.8	$1.1 \cdot 10^{-2}$	1.0

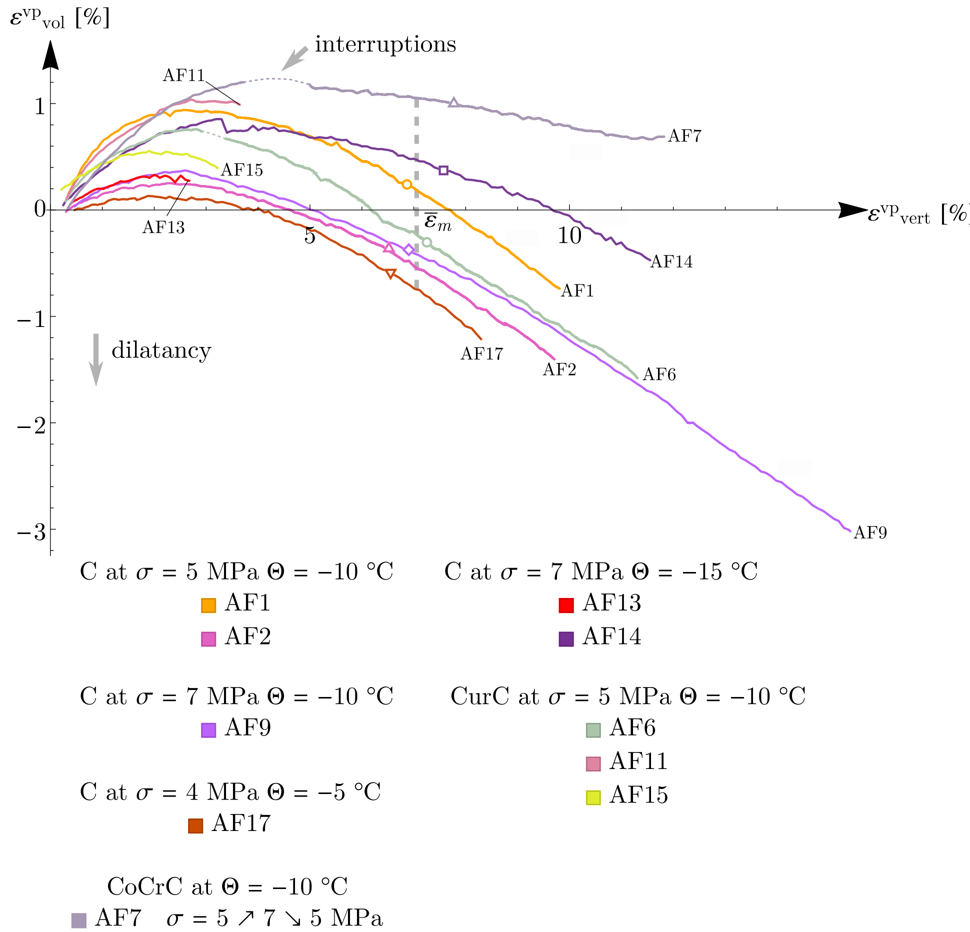

Figure 17: $\varepsilon^{\mathrm{vp}}_{\mathrm{vol}}(\varepsilon^{\mathrm{vp}}_{\mathrm{vert}})$ curves in C, CurC, CoCrC tests with indicated pairs $(\varepsilon_m, \varepsilon^{\mathrm{vp}}_{\mathrm{vol}}(\varepsilon_m))$ at $\dot{\varepsilon}_m$.

4.4.2. Displacement and deformation fields

A possible strain localization taking place during creep under uniaxial stress was refuted basing on the displacement and strain components obtained with the PIV as 2D fields. Time t was replaced by the average vertical strain component $\varepsilon^{\mathrm{vp}}$, i.e., $\mathbf{u}(\mathbf{X},\varepsilon^{\mathrm{vp}})$ and $\boldsymbol{\varepsilon}^{\mathrm{vp}}(\mathbf{X},\varepsilon^{\mathrm{vp}})$ are considered instead of $\mathbf{u}(\mathbf{X},t)$ and $\boldsymbol{\varepsilon}^{\mathrm{vp}}(\mathbf{X},t)$. Here, fields $\mathbf{u}(\mathbf{X},\varepsilon^{\mathrm{vp}})$ and $\boldsymbol{\varepsilon}^{\mathrm{vp}}(\mathbf{X},\varepsilon^{\mathrm{vp}})$ are presented in the form of contour plots in Fig. 18 and Fig. 19, respectively, for one face of sample AF1 at $\varepsilon^{\mathrm{vp}} \approx \varepsilon_m$ only. The displacement field $\mathbf{u}(\mathbf{X},\varepsilon^{\mathrm{vp}})$ includes the parallax error [23]. Nearly homogeneous deformation with no strain localization is observed.

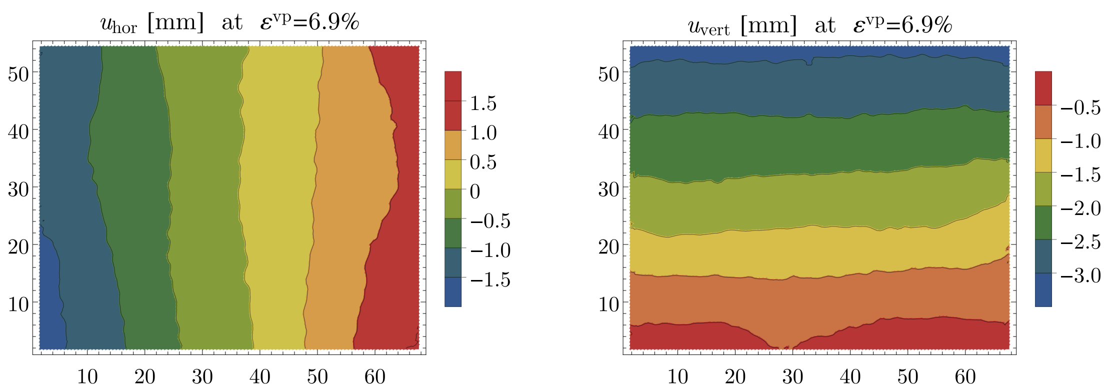

Figure 18: Horizontal $u_{\mathrm{hor}}(\mathbf{X},\varepsilon^{\mathrm{vp}})$ and vertical $u_{\mathrm{vert}}(\mathbf{X},\varepsilon^{\mathrm{vp}})$ components of displacement field for one face of sample AF1 at $\varepsilon^{\mathrm{vp}} \approx \varepsilon_m$.

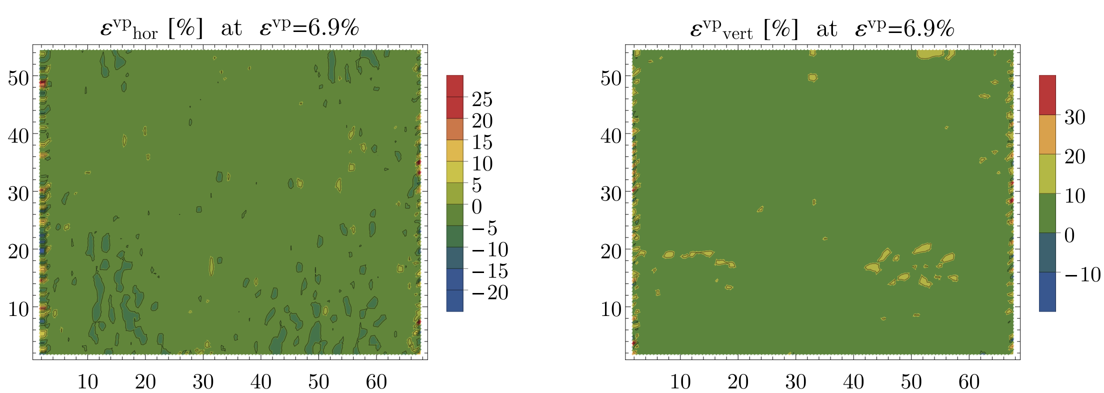

Figure 19: Horizontal $\varepsilon^{\mathrm{vp}}_{\mathrm{hor}}(\mathbf{X},\varepsilon^{\mathrm{vp}})$ and vertical $\varepsilon^{\mathrm{vp}}_{\mathrm{vert}}(\mathbf{X},\varepsilon^{\mathrm{vp}})$ components of deformation field for one face of sample AF1 at $\varepsilon^{\mathrm{vp}} \approx \varepsilon_m$.

4.5. Induced anisotropy of frozen soil

Due to the common use of the ground freezing technique in tunnel construction, the stress-induced anisotropy should be accounted for in a constitutive description of frozen soil.

A cubic sample that creeps under compressive stress $\sigma = \mathrm{const}$ applied in the material direction X_3 is schematically presented in Fig. 20a. The sample is assumed to be initially (inherently) isotropic. The loading direction is always vertical regardless of the material directions: X_1, X_2 and X_3. Before the minimum creep rate $\dot{\varepsilon}_m$ was achieved, the sample was quickly removed from the press and rotated, so that the loading direction was changed from X_3 to X_1, Fig. 20b. If the creep curve were regained after such operation, then the initial isotropy of the sample would be preserved. However, *induced anisotropy* of frozen soil was revealed in the CA tests carried out in this research.

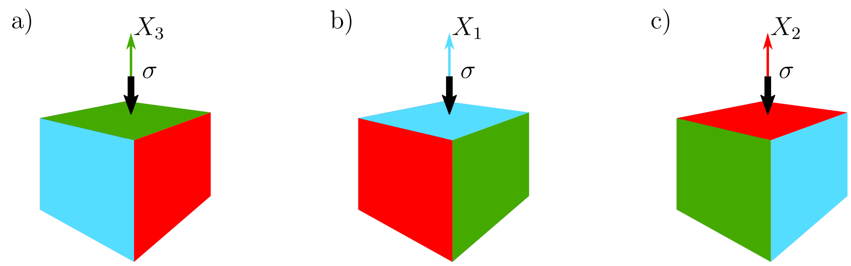

Figure 20: Cubic sample during creep under stress $\sigma = \mathrm{const}$ applied in different material directions: a) X_3; b) X_1; c) X_2.

5 CA tests on the cubic samples (A and AF) at $\sigma = 5$ MPa and $\Theta = -10$ °C are listed in Tab. 7. The sample loaded in different material directions in a CA test is shown in Fig. 20. Two types of the CA tests were conducted and are described below.

- In the first type, CA(1), the primary creep under $\sigma = 5$ MPa along X_3 was interrupted by unloading to $\sigma = 0$. The same stress $\sigma = 5$ MPa was then applied along X_1 and the sample creeped until the tertiary stage.

- In the second type, CA(2), the loading direction was changed in the primary stage first from X_3 to X_1 and then from X_1 to X_2.

Vertical creep strain at which the loading direction was changed is denoted as $\varepsilon_{\curvearrowright}^{\mathrm{vp}}$. Its values for the first ($\varepsilon_{\curvearrowright}^{\mathrm{vp}\,(1)}$) and for the second ($\varepsilon_{\curvearrowright}^{\mathrm{vp}\,(2)}$) change of the loading direction are reported in Tab. 7.

4.5.1. Tests with a single change of the loading direction (CA(1))

Directional dependence of the creep rate in tests on samples A5, AF5 and AF16

3 CA(1) tests on samples: A5, AF5 and AF16 are considered. In these tests, the loading $\sigma = 5$ MPa direction was changed from X_3 to X_1 at $\varepsilon_{\frown}^{\text{vp}\,(1)} = 2.9..3.7\% < \bar{\varepsilon}_m = 7.1\%$, see Tab. 7. The samples approached the tertiary creep stage under $\sigma = 5$ MPa applied along the second loading direction. The mean value of the vertical creep strain $\bar{\varepsilon}_m = 7.1\%$ at the slowest creep rate $\dot{\varepsilon}_m$ for the first loading direction is known from Sec. 4.3.4.

Creep curves, $\varepsilon^{\text{vp}}(t)$ and $\dot{\varepsilon}^{\text{vp}}(\varepsilon^{\text{vp}})$, for samples A5, AF5 and AF16 are shown in Fig. 21. A sample $\sqcup$ is denoted as $\sqcup(1)$ after the change of the loading direction, e.g., A5(1). The vertical creep strain, $\varepsilon^{\text{vp}}_{\text{vert}} \equiv \varepsilon^{\text{vp}}$, is $\varepsilon^{\text{vp}}_{33}$ before and $\varepsilon^{\text{vp}}_{11}$ after the change of the loading direction.

The strain $\varepsilon^{\text{vp}}_{11}$ includes the portion from the initial creep under $\sigma = 5$ MPa applied along X_3. This portion could be obtained for samples AF5 and AF16 from the PIV as the tensile horizontal strain, $\varepsilon^{\text{vp}}_{\text{hor}} \approx -1\%$, as can be seen later in Fig. 23a. It turned out to be reduced (almost to 0, see Fig. 21a) during application of the load in the new direction. This means that the creep strain increased by $\Delta\varepsilon^{\text{vp}}_{11} \approx 1\%$ already during the load application along the second direction. The creep strain increase $\Delta\varepsilon^{\text{vp}}_{33} \approx 0$ could be measured during the loading in the first direction [23]. Hence, the samples creeped significantly faster during the load application along the second direction compared to the first direction which already refutes isotropy of frozen soil.

Based on the PIV for samples AF5 and AF16, the vertical creep strain $\varepsilon^{\text{vp}} = 0$ was assumed for sample A5(1) (tested without the PIV) after the change of the loading direction. The curves $\dot{\varepsilon}^{\text{vp}}(\varepsilon^{\text{vp}})$ from Fig. 21 are additionally plotted in Fig. 22 together with the results from three similar C tests at the same $\sigma = 5$ MPa and $\Theta = -10$ °C.

It is clear in Fig. 22 that the creep rate $\dot{\varepsilon}^{\text{vp}}$ is not recovered after the change of the loading direction. Hence, isotropy of frozen soil is disproven. The minimum rate $\dot{\varepsilon}^{(1)}_m$ obtained for the second loading direction is about 2 times faster than $\dot{\varepsilon}_m$ expected for the first direction, see Fig. 22. Additionally, the strain $\varepsilon^{(1)}_m \approx 10\%$ at $\dot{\varepsilon}^{(1)}_m$ is different from the mean value $\bar{\varepsilon}_m = 7.1\%$ at $\dot{\varepsilon}_m$ corresponding to the first loading direction.

Anisotropy of frozen soil is most probably induced by changes in the microstructure during the creep. Their constitutive description requires a tensorial state variable and further lab investigation.

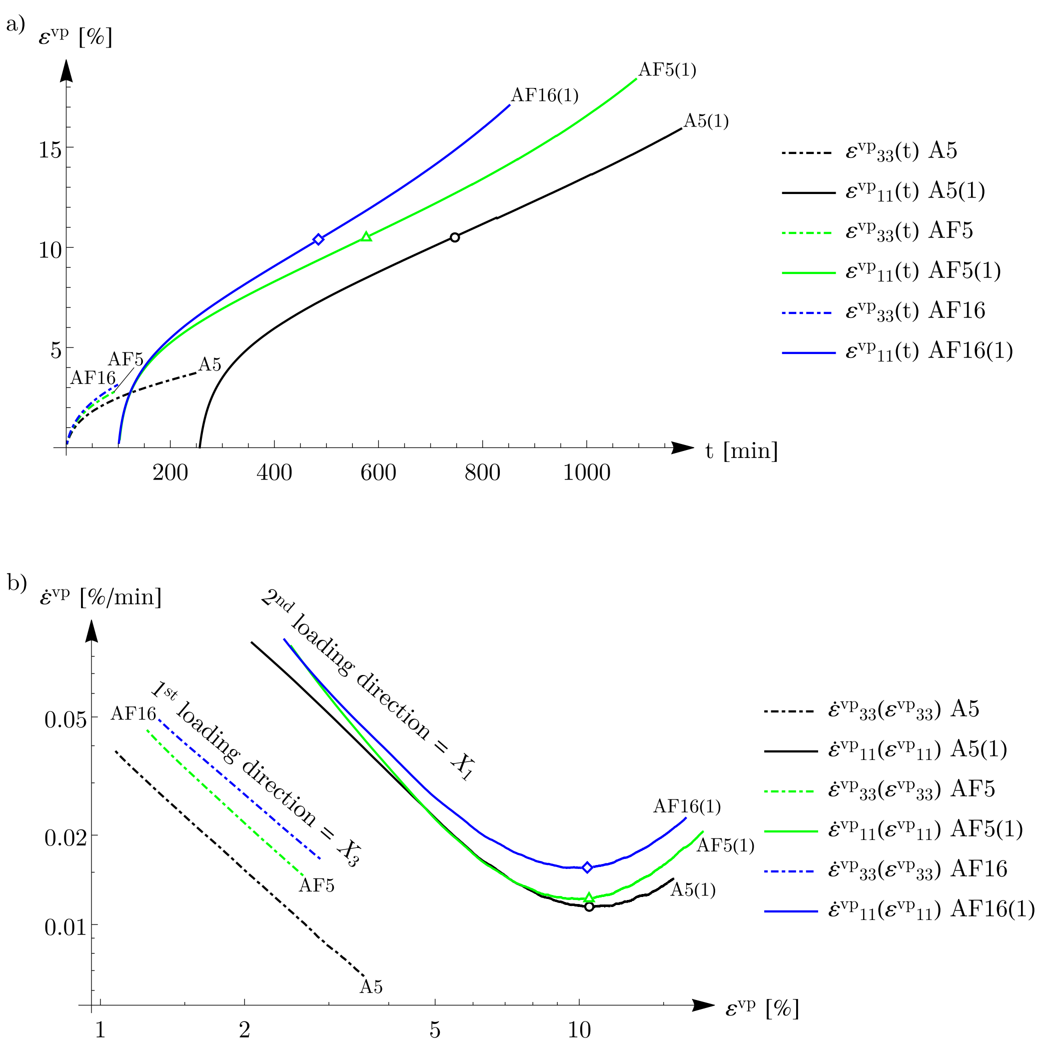

Figure 21: CA(1) tests A5, AF5 and AF16: a) $\varepsilon^{\mathrm{vp}}(t)$ curves with indicated inflections (”t_m”, ε_m) (Standing time has no meaning and hence is denoted as ”t_m”.); b) $\dot{\varepsilon}^{\mathrm{vp}}(\varepsilon^{\mathrm{vp}})$ curves with indicated minima (ε_m, $\dot{\varepsilon}_m$).

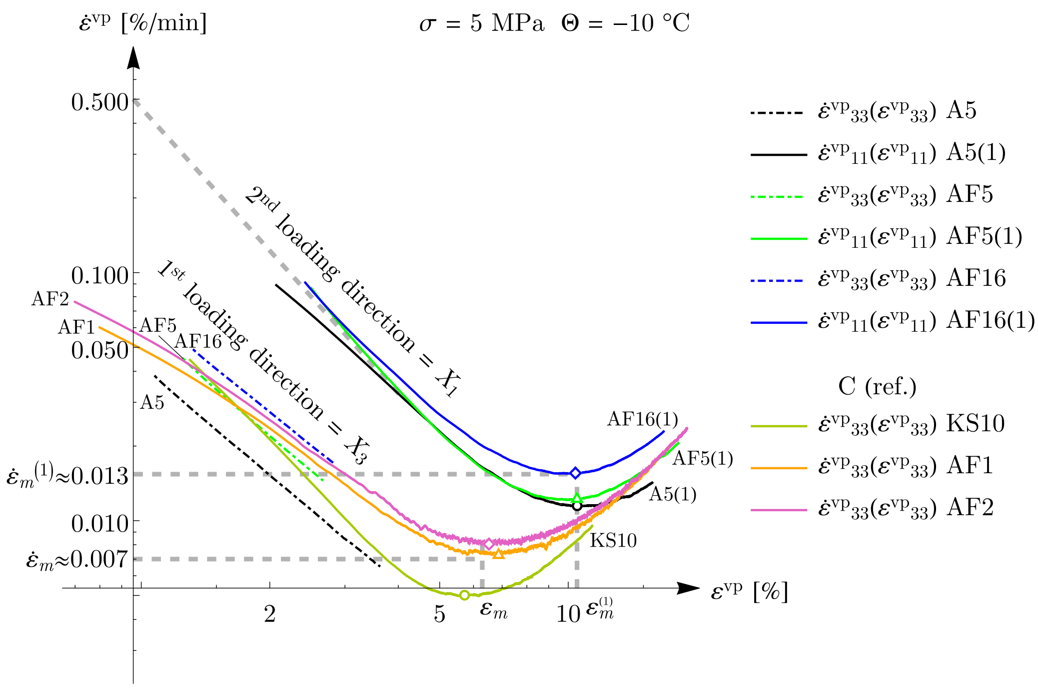

Figure 22: $\dot{\varepsilon}^{vp}(\varepsilon^{vp})$ curves in CA(1) tests A5, AF5, AF16 and the referential C tests with indicated minima ($\varepsilon_m,\ \dot{\varepsilon}_m$).

Dilatancy in tests on samples AF5 and AF16

Samples AF5 and AF16 were tested with the PIV. The dilatancy and the homogeneity of deformation within the samples after the change of the loading direction were observed. Unfortunately, no reliable results of PIV could be obtained for the whole tests due to the already mentioned pixel renegades. In the case of sample AF5(1), the horizontal strain $\varepsilon_{\mathrm{hor}}^{\mathrm{vp}}$ could be gained from the PIV on one sample face only because the images of the second face were blurred. After the change of the loading direction from X_3 to X_1 at $\varepsilon_{\mathrm{vert}}^{\mathrm{vp}} = \varepsilon_{\curvearrowright}^{\mathrm{vp}\,(1)}$, the horizontal strain increase $\Delta\varepsilon_{\mathrm{hor}}^{\mathrm{vp}}$ was measured via the PIV. It corresponds to the increases: $\Delta\varepsilon_{22}^{\mathrm{vp}}$ and $\Delta\varepsilon_{33}^{\mathrm{vp}}$ above the values of $\varepsilon_{22}^{\mathrm{vp}}$ and $\varepsilon_{33}^{\mathrm{vp}}$ at $\varepsilon_{\mathrm{vert}}^{\mathrm{vp}} = \varepsilon_{\curvearrowright}^{\mathrm{vp}\,(1)}$. Analogously, the volumetric strain increase $\Delta\varepsilon_{\mathrm{vol}}^{\mathrm{vp}}$ is considered instead of the total volumetric strain $\varepsilon_{\mathrm{vol}}^{\mathrm{vp}}$.

The strain paths for creep, $\varepsilon_{\mathrm{hor}}^{\mathrm{vp}}(\varepsilon_{\mathrm{vert}}^{\mathrm{vp}})$ and $\varepsilon_{\mathrm{vol}}^{\mathrm{vp}}(\varepsilon_{\mathrm{vert}}^{\mathrm{vp}})$, are presented for samples AF5 and AF16 before and after the change of the loading direction in Figs. 23–24. These results are additionally plotted with the ones from all other creep tests with the PIV (excluding the abnormal test AF7) from Sec. 4.4.

It can be seen in Fig. 24 that the samples AF5(1) and AF16(1) undergo the contractancy up to $\varepsilon_{\mathrm{vert}}^{\mathrm{vp}} \approx \frac{1}{2}\bar{\varepsilon}_m^{(1)}$, same as samples tested without a change of the loading direction, $\varepsilon_{\mathrm{vert}}^{\mathrm{vp}} \approx \frac{1}{2}\bar{\varepsilon}_m$. After that, the dilatancy can be observed and the sample volume exceeds the initial volume, described by $\varepsilon_{\mathrm{vol}}^{\mathrm{vp}} < 0$, at the slowest creep rate in the case of all samples.

The displacement components and the strain components obtained with the PIV and plotted as the fields on one wall of sample AF16(1), that is, after the change of the loading direction can be found in [23]. Distribution of the deformation is nearly homogeneous in the CA(1) tests, similarly as in the tests without a change of the loading direction.

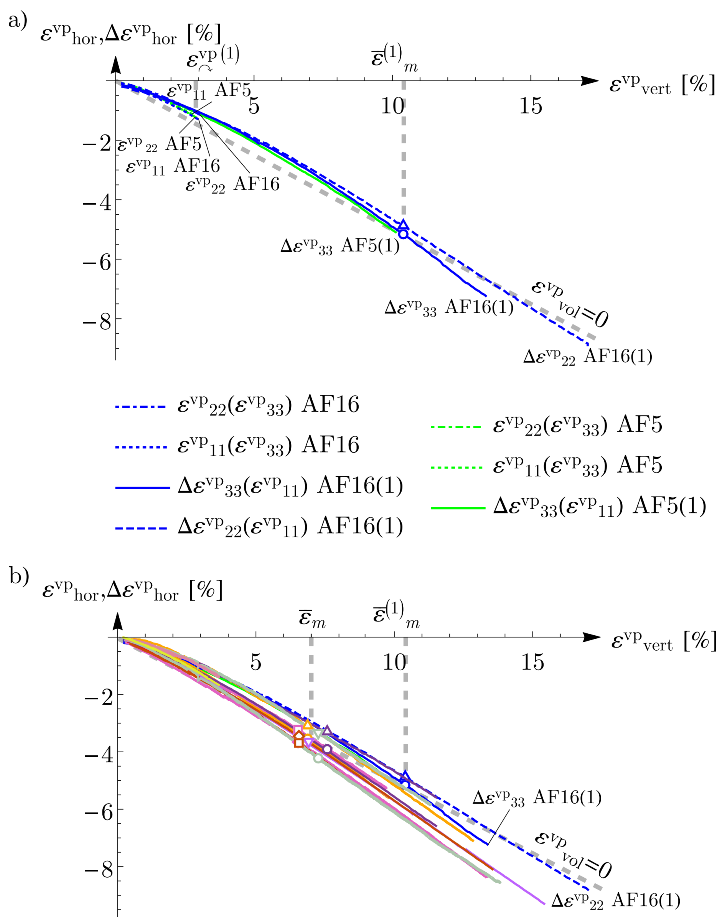

Figure 23: $\varepsilon^{\mathrm{vp}}_{\mathrm{hor}}(\varepsilon^{\mathrm{vp}}_{\mathrm{vert}})$ curves with indicated pairs $(\varepsilon_m, \varepsilon^{\mathrm{vp}}_{\mathrm{hor}}(\varepsilon_m))$ at $\dot{\varepsilon}_m$: a) in CA tests on samples AF5 and AF16; b) in CA tests on samples AF5 and AF16 and in all other creep tests with the PIV (excluding abnormal test AF7).

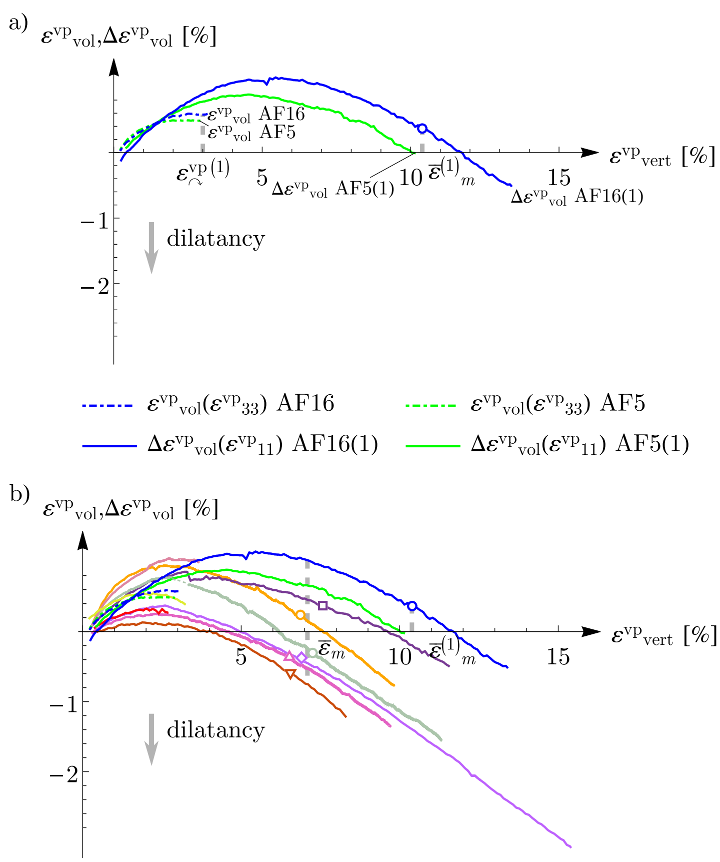

Figure 24: $\varepsilon^{vp}_{vol}(\varepsilon^{vp}_{vert})$ curves with indicated pairs $(\varepsilon_m, \varepsilon^{vp}_{vol}(\varepsilon_m))$ at $\dot{\varepsilon}_m$: a) in CA tests on samples AF5 and AF16; b) in CA tests on samples AF5 and AF16 and in all other creep tests with the PIV (excluding abnormal test AF7).

Directional dependence of the creep rate in test on sample A8 frozen with an initial stress state $\boldsymbol{\sigma}^{eff}$

Sample A8 was vertically preloaded (in direction X_3) before the freezing. This means it was frozen with an initial effective stress state $\boldsymbol{\sigma}^{\text{eff}} = \sigma^{\text{eff}}\text{diag}(1, \approx K_0, \approx K_0)$. The preload was applied by tighting the screws at the top plate of the preparation equipment [23]. For this purpose, a torque wrench was used and the axial force was assigned to the screws with the moment $M = 40$ Nm. The vertical prestress $\sigma^{\text{eff}} \approx 0.8$ MPa could be estimated using $M = 40$ Nm and the parameters of the screws.

The loading direction in the case of sample A8 was changed from X_3 to X_1 at $\varepsilon^{\text{vp}} = \varepsilon_{\frown}^{\text{vp}\,(1)} = 2.6\% < \bar{\varepsilon}_m = 7.1\%$, similarly as in the CA(1) tests on samples A5, AF5 and AF16, see Tab. 7. For this reason, the creep curves $\dot{\varepsilon}^{\text{vp}}(\varepsilon^{\text{vp}})$ are plotted for sample A8 together with the ones for samples A5, AF5 and AF16 in Fig. 25. The vertical creep strain $\varepsilon^{\text{vp}} = 0$ was assumed after the change of the loading direction based on the PIV for samples AF5 and AF16.

It is clear in Fig. 25 that the preload $\sigma^{\text{eff}} \approx 0.8$ MPa in direction X_3 affected the creep rate $\dot{\varepsilon}^{\text{vp}}$. The slower rate $\dot{\varepsilon}^{\text{vp}}$ was obtained for the preloaded sample A8 before the change of the loading direction as compared to the samples without the preloading. However, sample A8 demonstrates the same $\dot{\varepsilon}^{\text{vp}}$ as samples A5, AF5 and AF16 after the change of the loading direction. Unfortunately, the test on A8 was stopped before the tertiary stage was approached and hence the values of the minimum creep rate $\dot{\varepsilon}_m$ cannot be compared.

Systematic influence of the effective stress $\boldsymbol{\sigma}^{\text{eff}}$ on the slowest creep rate $\dot{\varepsilon}_m$ requires further lab investigation.

4.5.2. A test with two changes of the loading direction (CA(2))

In the CA(2) test on sample A7, the loading $\sigma = 5$ MPa direction was first changed from X_3 to X_1 at $\varepsilon^{\text{vp}} = \varepsilon_{\frown}^{\text{vp}\,(1)} = 4.9\% < \bar{\varepsilon}_m = 7.1\%$. The sample creeped under $\sigma = 5$ MPa until $\varepsilon^{\text{vp}} = \varepsilon_{\frown}^{\text{vp}\,(2)} = 5.2\% < \bar{\varepsilon}_m^{(1)}$, wherein $\bar{\varepsilon}_m^{(1)} \approx 10\%$ is known from the CA(1) tests. The loading direction was then changed from X_1 to X_2 and the sample approached the tertiary creep under $\sigma = 5$ MPa applied along X_2.

The diagrams $\dot{\varepsilon}^{\text{vp}}(\varepsilon^{\text{vp}})$ are shown in Fig. 26 together with the results from three CA(1) tests, A5, AF5 and AF16. Based on the PIV for samples AF5 and AF16, the strain $\varepsilon^{\text{vp}} = 0$ was assumed after the first change of the loading direction. Due to the lack of lab data, $\varepsilon^{\text{vp}} = 0$

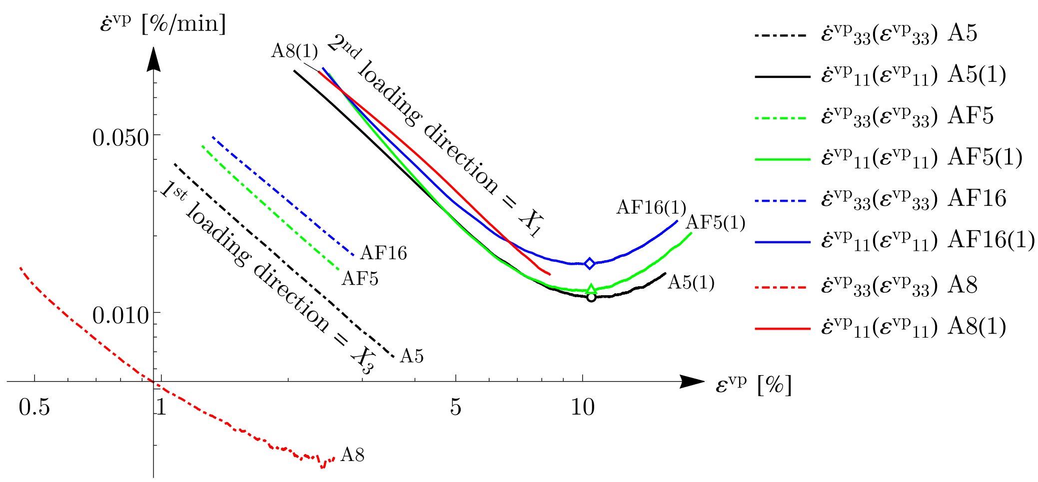

Figure 25: $\dot{\varepsilon}^{\mathrm{vp}}(\varepsilon^{\mathrm{vp}})$ curves in CA(1) tests A5, AF5, AF16 and A8 with indicated minima $(\varepsilon_m, \dot{\varepsilon}_m)$.

was assumed also after the second change of the loading direction.

Nearly the same curves $\dot{\varepsilon}^{\mathrm{vp}}(\varepsilon^{\mathrm{vp}})$ were obtained in the case of all samples for the first, X_3, and the second, X_1, loading direction, see Fig. 26. The rate $\dot{\varepsilon}^{\mathrm{vp}}$ corresponding to the third loading direction, X_2, is faster than the one corresponding to the first direction, X_3, but slower than the one corresponding to the second direction, X_1. The value of strain $\varepsilon_m^{(2)} = 5.9\%$ obtained at $\dot{\varepsilon}_m^{(2)}$ is only slightly different from the value expected for the initial loading direction $\bar{\varepsilon}_m = 7.1\%$.

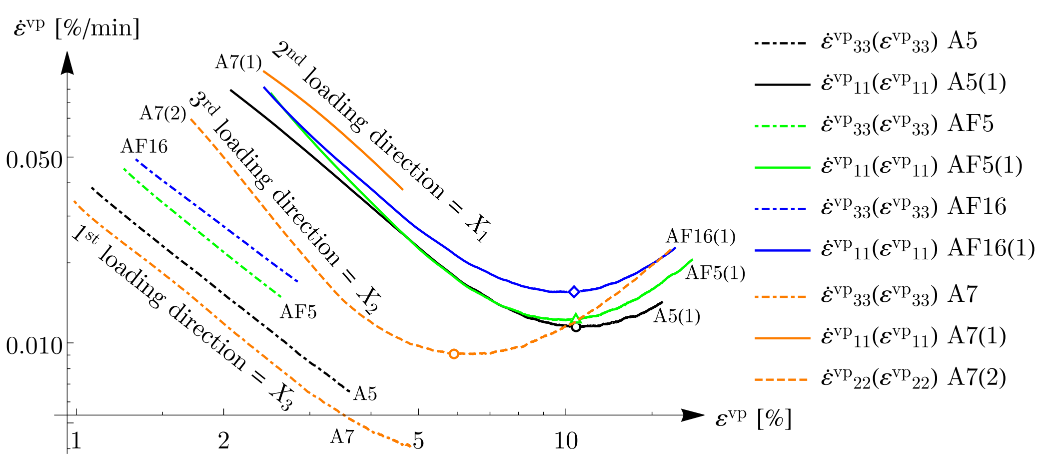

Figure 26: $\dot{\varepsilon}^{\mathrm{vp}}(\varepsilon^{\mathrm{vp}})$ curves in CA(2) test A7 and CA(1) tests A5, AF5 and AF16 with indicated minima $(\varepsilon_m, \dot{\varepsilon}_m)$.

Table 7: Summary of CA tests.

Sample/ Test	Material	Type of test	Θ °C	σ MPa	Loading direction	$\varepsilon^{\mathrm{vp}}_{\curvearrowright}$ %	ε_m %	$\dot{\varepsilon}_m$ %/min
A5	KFS	CA(1)	-10	5	X_3	3.7	-	-
A5(1)	KFS	CA(1)	-10	5	X_1	-	10.5	$1.1 \cdot 10^{-2}$
AF5	KFS	CA(1)	-10	5	X_3	2.9	-	-
AF5(1)	KFS	CA(1)	-10	5	X_1	-	10.5	$1.2 \cdot 10^{-2}$
AF16	KFS	CA(1)	-10	5	X_3	3.2	-	-
AF16(1)	KFS	CA(1)	-10	5	X_1	-	10.4	$1.6 \cdot 10^{-2}$
A8	KFS	CA(1)	-10	5	X_3	2.6	-	-
A8(1)	KFS	CA(1)	-10	5	X_1	-	-	-
A7	KFS	CA(2)	-10	5	X_3	4.9	-	-
A7(1)	KFS	CA(2)	-10	5	X_1	5.2	-	-
A7(2)	KFS	CA(2)	-10	5	X_2	-	5.9	$9.1 \cdot 10^{-3}$

5. Creep tests under isotropic compression

Observations on the purely volumetric creep of ice are possible in unsaturated samples [12]. It was shown that the volumetric creep of ice under isotropic pressure is due to the presence of air bubbles, Fig. 27. Unfortunately, there is lack of experimental results from the literature in the case of frozen soil. Purely volumetric creep of frozen soil is possible, if air bubbles are present. To the authors' knowledge, the volumetric deformation under isotropic stress is a rarely studied aspect of the constitutive description of creep in frozen soil.

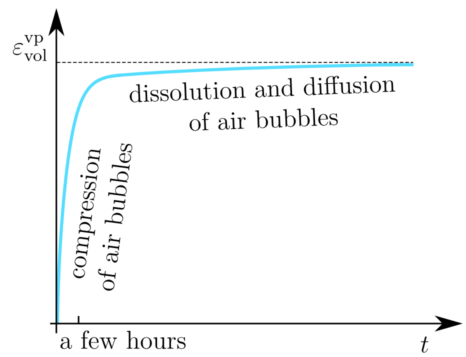

Figure 27: Volumetric strain $\varepsilon_{\mathrm{vol}}^{\mathrm{vp}}$ as function of time t for pure ice with air bubbles under isotropic pressure $p = \mathrm{const}$ applied at $t = 0$.

The volumetric creep of frozen sand was investigated under isotropic pressure in the course of this research [23, 35]. Samples were tested in a pressure vessel. Isotropic stress was applied on the sample through the cell fluid (hydraulic oil). Volumetric strain of the sample was determined by measuring the relaxation of the pressure in cell.

No acceleration of the creep rate, let alone the three stages of creep: primary, secondary and tertiary, were expected in the case of isotropic loading. It was attempted to verify and quantify the following hypotheses known from the tests on pure ice with air bubbles [12].

- Creep deformation during a quick load application can be neglected.
- No influence of the unfrozen water inside the frozen sample (around the grains) is taken into account. This is justified by relatively low values of the unfrozen water content $\mu^{\mathrm{w}} \leq 1\%$ in frozen sands [20].
- Within the first couple of hours, creep is mainly due to the compression of air bubbles. The initial atmospheric pressure p^{atm} inside a bubble increases up to the target pressure p and

the volume V^{a} of air bubbles decreases according to the Boyle-Mariotte law $pV^{\mathrm{a}} = \mathrm{const}$.

- Next, the compressed air bubbles are dissolved and diffuse slowly in the ice according to the Henry's law. For sufficiently high pressure, no bubbles will eventually be left which may take a few days.

- Finally, the frozen sand sample consists only of the almost incompressible substance (no air bubbles) and the volumetric deformation reaches asymptotically a limit.

5.1. *Tested material, sample preparation and experimental procedures*

Cylindrical samples with the diameter of 5 cm and the height of 10 cm were obtained by freezing KFS with different saturation. The size of samples was limited by the available testing device. Tests were conducted in the relaxation chamber placed in the cold room.

5.2. *Processing of data*

Temperature recordings and displacement of the piston into/out of the pressure vessel were provided by the data logger of the testing device. Values of pressure were read from the images of the manometer and manually appended to the experimental data. Raw lab measurements required correction for air bubbles in cell fluid. This correction was evaluated experimentally [23].

5.3. *Purely volumetric creep*

Samples were investigated at $\Theta = -10$ °C in the relaxation chamber filled with the hydraulic oil. The pressure $p_0 = 10$ MPa was applied inside the vessel and the visco-plastic volumetric strain $\varepsilon^{\mathrm{vp}}_{\mathrm{vol}}$ of the samples was obtained from the relaxation of the cell pressure, $\dot{p} < 0$.
3 tests on samples: P1, P2 and P7 with different values of the degree of saturation S are considered, see Tab. 8. Elastic response of the samples with the sample bulk modulus $K = \mathrm{const}$ was assumed during application of the load. Two steps of the load application were used. In the first step, the pressure was applied from $p = p^{\mathrm{atm}}$ to $p = 8$ MPa using the oil pump. In the second step, the pressure was increased from $p = 8$ MPa to $p = p_0 = 10$ MPa by screwing of the piston. The constant bulk modulus $K = 5.5$ GPa [16] was used for the pressure range $p = p^{\mathrm{atm}}..8$ MPa. The values of K (secant) for $p = 8..10$ MPa are given in Tab. 8. They were

calculated for each sample by subtracting the reference results from the test on a steel dummy sample conducted for the correction for air bubbles in oil, see [23].

The value of K increases with the degree of saturation S of the sample as it is observed in unsaturated soils with water. However, they are unrealistically low. This is probably due to a larger amount of the bubbles present in the oil in the considered tests than in the test on the dummy sample. Hence, all results obtained from the CI tests are fraught by the error due to the air bubbles in cell fluid.

Table 8: Summary of CI tests.

Sample/ Test	S -	K for $p = 8..10$ MPa MPa
P1	0.77	134
P2	0.82	416
P7	0.95	749

The purely volumetric creep deformation of the samples is shown as a time function $\varepsilon_{\mathrm{vol}}^{\mathrm{vp}}(t)$ in Fig. 28. It can be seen that initially the samples creeped fast with a nearly constant rate $\dot{\varepsilon}_{\mathrm{vol}} \approx$ const. Then, the creep slowed down and $\varepsilon_{\mathrm{vol}}^{\mathrm{vp}}$ achieved asymptotically a final constant value $\varepsilon_{\mathrm{vol\,max}}$. These observations are similar to the ones for pure ice [12]. The values of $\varepsilon_{\mathrm{vol\,max}}$ increase with the decreasing degree of saturation S.

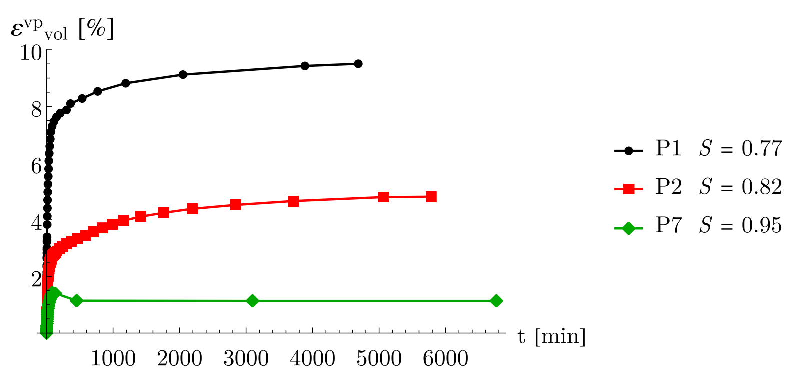

Figure 28: $\varepsilon_{\mathrm{vol}}^{\mathrm{vp}}(t)$ in the CI tests.

The physical interpretation of the purely volumetric creep of frozen soil pertains solely to the case of isolated air bubbles in the pore ice and corresponds roughly to the degree of saturation $S \gtrapprox 0.97$ [23]. Samples P1 and P2 with $S \ll 0.97$ have to be disregarded. Only sample P7 with $S = 0.95$ included solely isolated air bubbles and can be evaluated.

Note that a peculiar behaviour of sample P7 can be observed in Fig. 28. After the initial increase, the volumetric strain $\varepsilon_{\mathrm{vol}}^{\mathrm{vp}}$ decreased slightly before the final value $\varepsilon_{\mathrm{vol\,max}}$ was established. This could be caused by the relaxation of the cell pressure. The volumetric deformation $\varepsilon_{\mathrm{vol}}^{\mathrm{vp}}$ was initially dictated by p_0. The reduction of the bubbles (both in the sample and cell fluid) resulted in the relaxation $\dot{p} < 0$ but a certain amount of the bubbles was already dissolved in the ice. According to the Henry's law, less moles of the free air can be dissolved under the decreased p. Thus, the bubbles might have nucleated due to $\dot{p} < 0$.

Volumetric creep is due to the compression (or expansion) of air bubbles in frozen sample alone, similarly as it is in the case of pure ice [12]. Phenomena like dissolution, nucleation and diffusion of air bubbles in ice are rather negligible (about 250 times smaller than in water judging by the Henry constant [11]).

The purely volumetric and oedometric creep of frozen soil has been recently further investigated in the course of a master thesis at IBF, KIT [36].

6. Conclusions

Current evaluation of the creep deformation of artificially frozen soil should be revised. Constitutive models from the literature for frozen soil use explicit time functions. Direct time dependence depletes a constitutive description of the autonomity and generality. Application of the available models is thus restricted to uninterrupted creep only. A sound constitutive background for creep of frozen soil is of practical importance for the ground freezing technology. Formulation of an improved model requires novel lab evidence. For this purpose, different aspects of the creep of frozen soil were examined in the course of this research.

Frozen sand samples were investigated under uniaxial compression. Creep rate turned out to recover after any kind of interruptions, like unloadings or overloadings. In this way, a universal creep curve was established for frozen Karlsruhe Fine Sand.

Tests on cubic samples were conducted with the PIV. It allowed the quantification of the volumetric changes during creep under uniaxial stress. Contractancy and dilatancy of the sample were observed. Moreover, the distribution of deformation within the sample was judged from the 2D deformation fields on sample walls. No strain localization during creep could be observed.

Induced anisotropy of frozen soil was revealed in the tests with changes of the loading direction. Cubic sample under uniaxial stress was unloaded, rotated by 90° and reloaded back to the previous stress. Creep rate prior to the change of the loading direction was not regained.
Additionally, the creep tests under isotropic compression were carried out. Purely volumetric creep of frozen soil was shown to be due to the presence of air bubbles alone.
A refined material description is currently being developed. Novel model MROŻON for creep of frozen soil will account for the effective stress in soil skeleton and in ice.

Declarations

Funding

Not applicable

Conflicts of interest/Competing interests

Not applicable

Availability of data and material

All lab data can be obtained on an e-mail request.

Code availability

The relevant packages for the algebra program MATHEMATICA are available on an e-mail request.

Authors' contributions

Not applicable

References

[1] Chupin O, Rechenmacher A, Abedi S (2011) Finite strain analysis of nonuniform deformation inside shear bands in sands. International Journal for Numerical and Analytical Methods in Geomechanics 36(14):1651–1666, DOI 10.1002/nag.1071

[2] Cudmani R (2006) An elastic-viscoplastic model for frozen soils. In: Triantafyllidis T (ed) Numerical Modelling of Construction Processes in Geotechnical Engineering for Urban Environment, Taylor & Francis Group, pp 177–183

[3] Cudmani R, Yan W, Schindler U (2022) A constitutive model for the simulation of temperature-, stress- and rate-dependent behaviour of frozen granular soils. Géotechnique pp 1–36, DOI 10.1680/jgeot.21.00012

[4] Domaschuk L, Shields D, Rahman M (1991) A model for attenuating creep of frozen sand. Cold Regions Science and Technology 19:145–161

[5] Eckardt H (1979) Creep behaviour of frozen soils in uniaxial compression tests. Engineering Geology 13(1):185–195, DOI 10.1016/0013-7952(79)90031-0

[6] Eckardt H (1979) Tragverhalten gefrorener erdkörper. PhD thesis, Institut für Boden- und Felsmechanik, Universität Fridericiana in Karlsruhe, Heft Nr. 81

[7] Eckardt H (1982) Creep tests with frozen soils under uniaxial tension and uniaxial compression. In: Proceedings of the 4th Canadian Permafrost Conference, pp 394–405

[8] Fender K (2017) Low probability – high impact. Rail Engineer pp 34–38

[9] Fuentes Lacouture W (2014) Contributions in mechanical modelling of fill materials. Veröffentlichungen des IBF/KIT, Karlsruher Institut für Technologie, Heft 179

[10] Hassner T, Liu C (2016) Dense Image Correspondences for Computer Vision. Springer, Switzerland

[11] Ikeda-Fukazawa T, Fukumizu K, Kawamura K, Aoki S, Nakazawa T, Hondoh T (2005) Effects of molecular diffusion on trapped gas composition in polar ice cores. Earth and Planetary Science Letters 229(3):183–192, DOI 10.1016/j.epsl.2004.11.011

[12] Jones S, Johari G (1977) Effect of hydrostatic pressure on air bubbles in ice. In: Isotopes and Impurities in Snow and Ice, IAHS Redbooks, Gentbrugge, Belgium, vol 118, pp 23–28

[13] Knittel L (2020) Verhalten granularer böden unter mehrdimensionaler zyklischer beanspruchung. Veröffentlichungen des IBF/KIT, Karlsruher Institut für Technologie, Heft 188

[14] Liu Z, Yu X (2011) Coupled thermo-hydro-mechanical model for porous materials under frost action: Theory and implementation. Acta Geotechnica 6:51–65, DOI 10.1007/s11440-011-0135-6

[15] Ma L, Qi J, Yu F, Yao X (2015) Experimental study on variability in mechanical properties of a frozen sand as determined in triaxial compression tests. Acta Geotechnica 11, DOI 10.1007/s11440-015-0391-y

[16] Merz K, Vrettos C (2015) Aktuelle Forschung in der Bodenmechanik, chap Materialverhalten von gefrorenem Sand aus Triaxialversuchen an kubischen Proben, pp 101–117. DOI 10.1007/978-3-662-45991-1_6

[17] Orth W (1986) Gefrorener Sand als Werkstoff: Elementversuche und Materialmodell. PhD thesis, Institut für Boden- und Felsmechanik, Universität Fridericiana in Karlsruhe, Heft Nr. 100

[18] Orth W (2018) Grundbau-Taschenbuch Teil 2, John Wiley & Sons, chap 2.4 Bodenvereisung, pp 299–373. DOI 10.1002/9783433607312.ch4

[19] Orth W, Meissner H (1982) Long-term creep of frozen soil in uniaxial and triaxial tests. In: Proc. 3rdn Int. Symp. on Ground Freezing, Hanover, N.H., USA

[20] Osterkamp T, Burn C (2015) Cryosphere permafrost. In: North G, Pyle J, Zhang F (eds) Encyclopedia of Atmospheric Sciences (Second Edition), second edition edn, Academic Press, Oxford, pp 208–216, DOI 10.1016/B978-0-12-382225-3.00311-X

[21] Srokosz P, Bujko M, Bocheńska M, Ossowski R (2021) Optical flow method for measuring deformation of soil specimen subjected to torsional shearing. Measurement 174:109064, DOI 10.1016/j.measurement.2021.109064

[22] Staroszczyk R (2019) Ice Mechanics for Geophysical and Civil Engineering Applications. Springer, Switzerland

[23] Staszewska K (2022) Towards a constitutive description of creep in frozen soils. Dissertation, Gdańsk University of Technology, DOI 10.13140/RG.2.2.35977.11364

[24] Šuklje L (1957) The analysis of the consolidation process by the isotaches method. In: Proceedings 4th International Conference on Soil Mechanics and Foundation Engineering, Butterworths Scientific Publications, pp 200–206

[25] Ting J (1981) The creep of frozen sands: Qualitative and quantitative models. Massachusetts Inst of Tech Report

[26] Ting J (1983) On the nature of the minimum creep rate – time correlation for soil, ice, and frozen soil. Canadian Geotechnical Journal 20:176–182, DOI 10.1139/t83-017

[27] Vogelsang J (2017) Untersuchungen zu den mechanismen der pfahlrammung. Veröffentlichungen des IBF/KIT, Karlsruher Institut für Technologie, Heft 182

[28] White D, Take W, Bolton M (2003) Soil deformation measurement using particle image velocimetry (piv) and photogrammetry. Géotechnique 53(7):619–631, DOI 10.1680/geot.2003.53.7.619

[29] Wichtmann T (2016) Soil behaviour under cyclic loading - experimental observations, constitutive description and applications. Veröffentlichungen des IBF/KIT, Karlsruher Institut für Technologie, Heft Nr 181 (habilitation)

[30] Wolfram Research Inc (2021) Mathematica

[31] Xu X, Wang Y, Zhenhua Y, Zhang H (2017) Effect of temperature and strain rate on mechanical characteristics and constitutive model of frozen helin loess. Cold Regions Science and Technology 136, DOI 10.1016/j.coldregions.2017.01.010

[32] Yao X, Wang W, Zhang M, Wang S, Wang L (2021) Strain localization of a frozen sand under different test conditions. Cold Regions Science and Technology 183:103226, DOI 10.1016/j.coldregions.2021.103226

[33] Zachert H (2015) Zur gebrauchtauglichkeit von gründungen für offschore-windenergieanlagen. Veröffentlichungen des IBF/KIT, Karlsruher Institut für Technologie, Heft 180

[34] Zhou G, Zhou Y, Hu K, Wang Y, Shang X (2018) Separate-ice frost heave model for one-dimensional soil freezing process. Acta Geotechnica 13, DOI 10.1007/s11440-017-0579-4

[35] Zürn J (2021) Volumetrisches Kriechverhalten in gefrorenem Sand. Karlsruher Institut für Technologie

[36] Zürn J (2022) Volumetrisches und ödometrisches Kriechverhalten in gefrorenem Sand. Master's thesis, Karlsruher Institut für Technologie